

# Precipitation of radiation belt electrons induced by obliquely propagating lightning-generated whistlers

D. S. Lauben, U. S. Inan and T. F. Bell

Space, Telecommunications and Radioscience Laboratory, Stanford University, Stanford, California

**Abstract.** A new combined ray tracing and test particle formulation is presented which calculates the spatiotemporal electron precipitation flux signatures at ionospheric altitudes induced by obliquely propagating lightning-generated whistler waves. The formulation accounts for the variation in wave characteristics (frequency-time dispersion, wave normal angle, and power density) as the whistler generated by an individual lightning discharge propagates through vast volumes of the magnetosphere in the absence of field-aligned cold plasma density enhancements, and calculates the detailed gyroresonance scattering of trapped energetic electrons into the atmospheric loss cone over a broad range of field lines ( $L$  shells) to determine the precipitation flux over extensive ionospheric regions. Results show that peak precipitation flux patches (hotspots) several tens of degrees of latitude and longitude in size develop at locations  $\sim 7^\circ$  to  $\sim 20^\circ$  poleward of the discharge as a consequence of propagation paths which convey wave energy from lower to higher  $L$  shells. For oblique whistler intensities matching satellite observations (10 to 30 pT) peak flux levels of several  $\text{milli-ergs cm}^{-2} \text{ s}^{-1}$  are indicated, arriving as early as  $\sim 1/4$  s and lasting  $\sim 1/2$  s at lower observing latitudes (e.g.,  $\sim 32^\circ$  for North American longitudes), while being delayed to  $\sim 1$  s or more and lasting up to  $\sim 2$  s at higher latitudes ( $\sim 47^\circ$ ), creating a sense of poleward hotspot motion. Summary profiles integrated over time, latitude and  $L$  shell suggest that lightning-generated oblique whistler-induced electron precipitation deposits appreciable energy to the upper atmosphere at midlatitudes and contributes significantly to the loss of energetic ( $>100$  keV) radiation belt electrons, particularly over  $2.2 \leq L \leq 3.5$  where the slot region forms.

## 1. Introduction

### 1.1. Wave-Induced Radiation Belt Losses

Since the discovery of the Earth's radiation belts [Van-Allen *et al.*, 1959], much progress has been made in understanding the source and loss processes controlling the fluxes of these highly energetic (100 eV to  $>100$  MeV) particles (for an overview the reader is referred to articles by Walt [1997] and McIlwain [1997]). Early attempts to understand the balance of mechanisms governing the equilibrium densities of radiation belt particles, particularly loss mechanisms, quickly recognized that Coulomb collisions with atmospheric constituents alone could not account for the observed loss rates throughout the majority of the magnetosphere. Furthermore, detailed satellite surveys during sustained periods of relatively quiet magnetospheric conditions revealed a peculiar density depletion or "slot" region at

several Earth radii appearing regularly over the course of only a few days following particle injection events [Lyons and Kennel, 1972], indicating the operation of some loss mechanism exhibiting pronounced selectivity over certain energy ranges for particular field lines.

**1.1.1. Incoherent and coherent waves.** These and similar observations led Dungey [1963], Cornwall [1964], and others to suggest that the coherent electromagnetic wave fields comprising lightning-generated whistlers might be particularly effective at scattering energetic electrons in pitch angle via cyclotron resonance interaction, possibly leading to the high particle loss rates considering the continual occurrence of lightning on a global scale. Soon thereafter, Kennel and Petschek [1966], successors Lyons and Thorne [1973], and others proposed a companion mechanism wherein a form of turbulent incoherent wave energy termed hiss would also, through many successive random-walk particle scatterings, lead to enhanced pitch angle diffusion and high particle loss rates, especially noting that hiss regularly occurs following disturbed magnetospheric conditions associated with injection events, and demonstrating that such models could be tuned to

account for the formation of the slot region. A later variation on the early coherent wave mechanism considered pitch angle scattering with signals from ground-based VLF transmitters; details of this interaction are addressed by *Inan et al.* [1978], *Koons et al.* [1981] and *Vampola and Adams* [1998].

Since the coherent and incoherent wave mechanisms both make appeal to the same general condition for wave-particle gyroresonance [*Brice*, 1964; *Dysthe*, 1971], they necessarily select the same resonant particle energies for the same combination of resonance order, wave frequency, wave normal angle, and magnetic field and latitude. Consequently, careful attention must be paid to the occurrence statistics and precise effects of all forms of wave energy present in the magnetosphere to properly account for the observed radiation belt dynamics. To this end, *Abel and Thorne* [1998a, b] have recently presented results suggesting that hiss, oblique-mode lightning-generated whistlers and VLF transmitter signals each play an important role within particular regimes in energy/field line/pitch angle parameter space. Most notably, their results show that oblique whistlers must be included for a complete treatment.

**1.1.2. Lightning-induced electron precipitation.** Using the SEEP detector aboard the S81-1 satellite, *Voss et al.* [1984] showed the association of strong ( $\sim 100\times$  background), transient ( $\sim 1$  s) enhancements to the precipitating energetic electron flux with individual lightning-generated whistlers, thus establishing lightning-induced electron precipitation (LEP) as both detectable and appreciable on an event-by-event basis. For instance, estimates based on these observations indicate that a single LEP burst can empty  $\sim 0.001\%$  of the radiation belt energetic electron population along the affected field line, depositing an energy fluence of  $\sim 10^{-3}$  ergs/cm<sup>2</sup> to the upper atmosphere, in turn leading to at least one form of the so-called “Trimpi” effect seen frequently on manmade subionospheric VLF/LF signals [*Carpenter et al.*, 1984; *Inan et al.*, 1985a; *Inan and Carpenter*, 1986; *Burgess and Inan*, 1993].

For further reference, the significance of wave-particle interactions in determining the loss rates for radiation belt energetic electrons, and in particular the role of burst precipitation events such as LEPs, has been discussed in detail by *Imhof et al.* [1983, 1986, 1989], *Vampola and Gorney* [1983], *Chang and Inan* [1985], *Burgess and Inan* [1993], *Walt et al.* [1996], *Imhof et al.* [1997], and others, while the relative role played by short-duration coherent wave packets as compared with sustained incoherent wave activity (e.g., VLF/ELF hiss) has been addressed by *Inan et al.* [1982], *Inan* [1987], and most recently by *Abel and Thorne* [1998a, b]. Regarding the effects of electron precipitation bursts on the upper atmosphere and perturbations to subionospheric ELF/VLF waves, the reader is referred to *Inan et al.* [1985, 1988, 1990, and references therein].

**1.1.3. Burst precipitation models.** Efforts to model burst precipitation events induced by discrete VLF

wave pulses progressed with *Inan et al.* [1978], *Chang et al.* [1983], and *Inan et al.* [1985], leading to *Inan et al.* [1989] which presented simulated energy-time precipitation spectra to match a single event taken from *Voss et al.* [1984]. In that case the responsible whistler wave energy was taken to have propagated in the so-called ducted mode, parallel to the particular magnetic field line during its traverse through the magnetosphere [*Helliwell*, 1965; *Carpenter et al.*, 1971] by virtue of its emergence from the magnetosphere in the hemisphere conjugate to the lightning source.

While these models were successful, the inherent restriction to ducted waves precludes treatment of the far greater portion of whistler wave energy propagating throughout vast volumes of the magnetosphere in the oblique mode at nonzero wave normal and ray path angles with respect to the Earth's field lines and thus not confined to isolated  $L$  shells. To address this general case, a new formulation is developed which calculates the electron precipitation over an entire hemisphere induced by such obliquely propagating whistlers whose characteristics match in situ observations as generated by individual lightning discharges of specified strength and location [*Lauben*, 1998]. The resulting precipitation fluxes strongly suggest that lightning-generated oblique whistler precipitation leads to appreciable energy deposition to the upper atmosphere and contributes significantly to the loss of energetic radiation belt electrons from the magnetosphere, particularly over the range  $2.2 \leq L \leq 3.5$  where the slot region forms.

## 1.2. LEP By Oblique Whistlers

**1.2.1. Canonical event sequence.** In assessing the transient electron precipitation induced by individual lightning-generated oblique whistlers over large ionospheric regions, it is expedient to first calculate the precipitation at the foot of individual magnetic field lines separately and combine results afterward. Accordingly, Plate 1 illustrates the canonical event sequence along a typical field line:

1. Impulsive broadband VLF electromagnetic wave energy radiated by a single lightning discharge (modeled as a vertically oriented dipole) spreads throughout the Earth-ionosphere waveguide, suffering subionospheric attenuation and absorption consistent with multimode waveguide models [*Poulsen et al.*, 1993].

2. A fraction of this wave energy couples through the horizontally stratified ionosphere over a wide range of latitudes and longitudes, exciting a whistler-mode wave packet which propagates obliquely throughout vast volumes of the smoothly varying magnetosphere, suffering additional frequency-dependent spatial refraction, attenuation and temporal dispersion to form an oblique whistler [*Lauben*, 1998; *Lauben et al.*, 1999].

3. As this discrete oblique whistler illuminates the field line, a fraction of the otherwise trapped energetic electrons initially near the edge of the atmospheric loss

cone matching the condition for Doppler-shifted gyroresonance (given below) become scattered into the loss cone.

4. The lowered mirror height of those particles deflected into the loss cone allows them to be precipitated at their next encounter with the relatively dense upper atmosphere.

As a result of the ubiquitous propagation of each oblique whistler throughout the magnetosphere, scattering occurs over a broad range of field lines leading to precipitation at ionospheric altitudes over a wide range of latitudes generally northward and southward of the lightning source. In addition, precipitation also occurs over a wide range of longitudes to either side of the meridian containing the lightning source, diminishing at a moderate rate with increasing longitudinal displacement from the source in accordance with the assumed lightning dipolar wave radiation pattern and subionospheric attenuation. Each lightning discharge thus leads to an associated transient precipitation event depositing flux over an extensive two-dimensional ionospheric area. In general, a large fraction will backscatter and undergo multiple bounces along the field line within the loss cone before being finally depleted; for simplicity herein all electrons are treated as lost to the atmosphere at their first encounter.

**1.2.2. Test-particle formulation.** The present formulation takes as precedent that of *Chang and Inan* [1985] for the precipitation at the foot of a single field line for discrete ducted whistler propagation along that same field line, and of *Ristic-Djurovic et al.* [1998] for test-particle gyroresonance with obliquely propagating but steady state monochromatic waves. In combining and extending these formulations to cover the general case of discrete obliquely propagating whistlers, further challenge is encountered in two areas:

i. The first area regards the interaction of a test particle with prevailing transient, frequency-dispersing oblique wave fields along its trajectory. Here the basic equations of motion for oblique-mode gyroresonance developed by *Bell* [1984] (given below) and first implemented by *Jasna et al.* [1992] and most recently by *Jasna et al.* [1998] (the later which treats the single-pass interaction of an ensemble of energetic electrons through monochromatic steady state oblique-mode wave fields) must be adapted to accommodate the

transient nature of the discrete oblique whistler wave packet.

ii. The second area regards specification of the transient oblique wave fields at all points along the field lines of interest arising from an individual lightning dis-

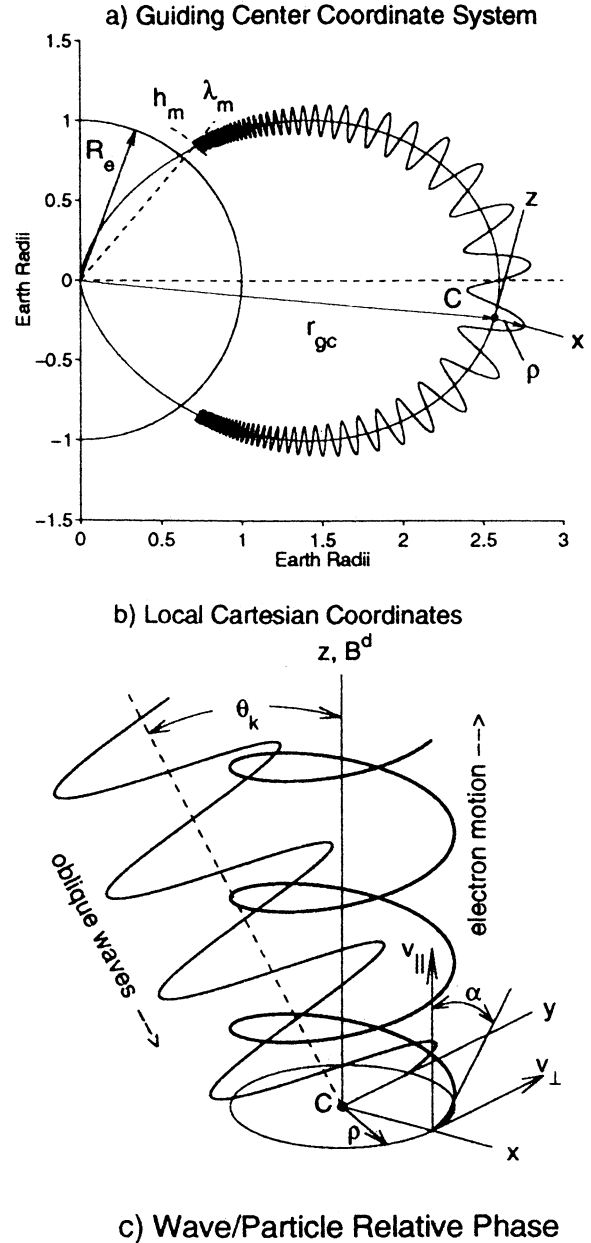


**Figure 1.** (a) Local Cartesian coordinate system at each point  $C=(L,\lambda)$  along the field line corresponding to guiding center  $r_{gc}$ . (b) Energetic electron helix in local Cartesian frame in which the elliptically polarized wave fields are applied. The wave normal angle  $\theta_k$  lies in the  $x$ - $z$  plane. (c) Gyroaveraged angle  $\eta$  between particle velocity vector  $v_{\perp}$  (at Larmor phase  $\varphi$ ) and the transverse right-hand circularly polarized wave magnetic field vector  $B_R^w = 1/2 (\hat{x}B_x^w + \hat{y}B_y^w)$  at wave phase  $\Phi$ .

charge at a given location. As no closed-form expression for the required oblique whistler wave characteristics (wave normal angle, wave power density, and propagation delay) exists, a comprehensive VLF ray tracing methodology is employed to establish these properties.

The general relativistic equation of motion for a test particle having rest mass  $m$  and charge  $q$  in the combined Earth dipole  $\mathbf{B}_o$  and oblique whistler-wave electromagnetic  $\mathbf{E}^w, \mathbf{B}^w$  fields may be written

$$\ddot{\mathbf{r}} = \frac{q}{m\gamma} [\mathbf{E}^w + \dot{\mathbf{r}} \times (\mathbf{B}_o + \mathbf{B}^w)], \quad (1)$$

where  $\gamma = 1/\sqrt{1-v^2/c^2}$  for total particle velocity  $v = |\dot{\mathbf{r}}|$ , with  $\mathbf{r}$  measured in the rest frame. In the absence of the wave fields ( $\mathbf{E}^w, \mathbf{B}^w=0$ ) this equation specifies classic adiabatic magnetic mirroring for which the path traced by a particle consists of cyclotron motion about the static field line  $\mathbf{B}_o$  plus linear translation along  $\mathbf{B}_o$ , which when superposed forms a helix conforming to the field line as depicted in Figure 1a. Such helix has local gyroradius  $\rho = m\gamma v_\perp/qB$  and pitch angle  $\alpha = \tan^{-1} v_\perp/v_\parallel$ , where  $v_\perp$  and  $v_\parallel$  are the particle velocities transverse and parallel to  $\mathbf{B}_o$ , both of which vary with local field strength  $B(\lambda) = |\mathbf{B}_o|$  according to [e.g., *Walt*, 1994, pp.42-43]

$$v_\parallel = v \cos \alpha(\lambda), \quad v_\perp = v \sin \alpha(\lambda) \quad (2a)$$

$$\sin^2 \alpha(\lambda) = (B(\lambda)/B_{eq}) \sin^2 \alpha_{eq}, \quad (2b)$$

where  $B_{eq}$  and  $\alpha_{eq}$  denote equatorial values. For a given value of  $\alpha_{eq}$ , mirroring occurs at that  $\lambda_m$  for which  $\alpha(\lambda_m) \rightarrow 90^\circ$ , defined implicitly by  $B(\lambda_m) = B_{eq}/\sin^2 \alpha_{eq}$ . The dipole geometry and field strength for a given field line are given respectively by

$$R(L, \lambda) = L \cos^2 \lambda \quad (3a)$$

$$B(L, \lambda) = B_\oplus \frac{1}{L^3} \frac{\sqrt{1+3\sin^2 \lambda}}{\cos^6 \lambda}, \quad (3b)$$

where  $R$  is the radius to points at latitude  $\lambda$  along a given field line,  $L$  is equal to the geocentric distance at which the field line intersects the magnetic equator ( $R$  and  $L$  in Earth radii), and  $B_\oplus$  is the equatorial field strength at the Earth's surface, taken as  $B_\oplus = 3.12 \times 10^{-5}$  T. Then given some effective ionospheric height  $h_p$  above which particles are assumed free to mirror but below which they are considered lost due to atmospheric collisions (that is, precipitated) the corresponding equatorial loss cone pitch angle at the magnetic equator  $\alpha_{eq}^{lc}$  is given by *Inan* [1977]

$$\sin \alpha_{eq}^{lc} = \left[ \epsilon_m^3 / \sqrt{1+3(1-\epsilon_m)} \right]^{1/2}, \quad (4)$$

where  $\epsilon_m = (1/L)(R_e + h_m)/R_e$  and  $R_e = 6370$  km. Hence, in this basic model, the quiescent equatorial energetic particle distribution is taken as nonzero for pitch angles  $\alpha_{eq} \geq \alpha_{eq}^{lc}$  but void for  $\alpha_{eq} < \alpha_{eq}^{lc}$ , whereupon the

presence of the whistler wave fields causes a fraction of the electrons to be scattered to (equatorial) pitch angles  $\alpha_{eq} < \alpha_{eq}^{lc}$ , giving rise to precipitation. As an example, for  $L=2$  and  $h_p=100$  km, the equatorial loss cone pitch angle is  $\alpha_{eq}^{lc} \sim 16.8^\circ$ , and for a particle initially at this pitch angle and subsequently scattered by  $\sim 0.2^\circ$  into the loss cone, the mirror altitude is reduced to  $h'_p = 60$  km, well within the relatively dense upper atmosphere.

**1.2.3. Gyroaveraged equations of motion.** At each point  $C=(L, \lambda)$  along the field line, a local cartesian coordinate system with  $\hat{\mathbf{z}} \parallel \mathbf{B}_o$  and  $\hat{\mathbf{x}}$  pointing towards higher  $L$  provides a reference frame for the electron helix and wave field components as shown in Figures 1a and 1b. *Bell* [1984] gives the equations of motion developed from (1) for an energetic electron in terms of the particle velocity  $v_\parallel, v_\perp$  parallel and perpendicular to  $\hat{\mathbf{z}}$  and the gyroperiod-averaged phase angle  $\eta$  between the particle velocity vector, at Larmor phase  $\varphi$ , and the suitably decomposed right-hand circularly polarized component  $\mathbf{B}_R^w = 1/2(\hat{\mathbf{x}}B_x^w + \hat{\mathbf{y}}B_y^w)$  of the wave total magnetic field vector  $\mathbf{B}^w$ , itself at generalized wave phase  $\Phi = \int \omega dt - \int \mathbf{k} \cdot d\mathbf{r}$  [cf. *Bell*, 1984; *Jasna et al.*, 1993; and Figures 1b and 1c]

$$\dot{v}_\parallel = \frac{\omega_\tau^2}{m\gamma} k_z^{-1} \sin \eta - \frac{v_\perp^2}{2\omega_h} \frac{\partial \omega_h}{\partial z}, \quad (5a)$$

$$\dot{v}_\perp = -[\omega_1(v_z + R_1)J_0(\beta) - \omega_2(v_z - R_2)J_2(\beta)] \sin \eta + \frac{v_z v_\perp}{2\omega_h} \frac{\partial \omega_h}{\partial z}, \quad (5b)$$

$$\dot{\eta} = \frac{\omega_h}{\gamma} - \omega - k_z v_\parallel, \quad (5c)$$

where  $\omega$  is the instantaneous whistler wave frequency,  $\omega_h/\gamma = qB^o/m\gamma$  is the local relativistic gyrofrequency of the energetic electron, and

$$\beta = k_x v_\perp / \omega_h,$$

$$k_z = k \cos \theta_k = \frac{\omega}{c} n(\theta_k) \cos \theta_k,$$

$$k_x = k \sin \theta_k = \frac{\omega}{c} n(\theta_k) \sin \theta_k,$$

$$\omega_\tau^2 = \omega_{\tau o}^2 [J_0(\beta) - \alpha_1 J_2(\beta) + \gamma \alpha_2 J_1(\beta)],$$

$$\omega_{\tau o}^2 = \omega_1 k_z v_\perp,$$

$$\omega_{1,2} = (q/2m_e)(B_x^w \pm B_y^w),$$

$$\alpha_1 = \omega_1/\omega_2,$$

$$\alpha_2 = qE_z^w/(m\gamma\omega_1 v_\perp),$$

$$R_{1,2} = (E_x^w \pm E_y^w)/(B_x^w \pm B_y^w),$$

where  $n(\theta_k)$  is the refractive index for wave normal angle  $\theta_k$  with respect to  $\hat{\mathbf{z}}$  (Figure 1b and Section 2), and  $J_{0,1,2}$  are Bessel functions of the first kind. Especially important is the value of  $k_z$  in the fundamental resonance condition found by setting (5c) equal to zero so that the time rate of change of the angle  $\eta$  (Figure 1c) is nominally zero

$$\dot{\eta} = \omega_h/\gamma - w - k_z v_z = 0, \quad (6) \quad \text{total refractive index is given by}$$

When this condition is satisfied the Doppler-shifted frequency of the wave as seen by the energetic particle is matched to the particle's cyclotron frequency, and the gyroaveraged electromagnetic wave fields appear temporarily stationary in the particle frame. When this match prevails for some appreciable distance (or equivalently, time) along the field line, appreciable cumulative scattering can take place depending on the particular value of  $\eta$  in (5a) and (5b) unique to each particle.

Substituting  $\gamma = (1 - v^2/c^2)^{-1/2}$  with  $v^2 = v_z^2/\cos^2 \alpha$  (where  $\alpha$  is local particle pitch angle) and solving the resulting quadratic equation for parallel velocity yields the condition for oblique-wave gyroresonance

$$v_{\text{res}} = \frac{-\omega k_z \pm \sqrt{\omega^2 k_z^2 + (\omega_h^2 - \omega^2) \left( k_z^2 + \frac{\omega_h^2}{c^2 \cos^2 \alpha} \right)}}{k_z^2 + \frac{\omega_h^2}{c^2 \cos^2 \alpha}}, \quad (7)$$

The value of  $v_{\text{res}}$  indicates the parallel velocity which a particle must have in order to be in resonance with the wave, where in general all quantities are understood to be functions of magnetic latitude  $\lambda$  along the  $L$  shell to which the particle guiding center is bound. The plus or minus sign on the radical indicates resonance for particles either approaching (positive root) or overtaking (negative root) the wave, the former which includes electron energies in the keV to MeV range, the later which is limited mostly to the MeV range. Following previous formulations, counterstreaming electrons (positive root) are considered herein, for which the generally lower resonant energies permit more appreciable scattering for equivalent wave intensities.

**1.2.4. Oblique whistler wave fields.** The wave fields  $\mathbf{E}^w$ ,  $\mathbf{B}^w$  at each point  $C$  are developed after *Stix* [1962], where for a general magnetoplasma described by a suitably defined anisotropic dielectric tensor  $\bar{\mathbf{K}}$  for static field  $\mathbf{B}_0$ , the phasor solution to the time harmonic Maxwell equations

$$\begin{aligned} \nabla \times \mathbf{E} &= -j\omega \mathbf{B}, \\ \nabla \times \mathbf{B} &= (j\omega/c^2) \bar{\mathbf{K}} \mathbf{E}, \end{aligned}$$

gives electromagnetic field component ratios expressed in the coordinate system of Figure 1b

$$\begin{aligned} \frac{E_y}{E_x} &= \frac{iD_s}{S_s - n^2}, \quad \frac{E_z}{E_x} = \frac{n_x n_z}{n_s^2 - P_s}, \\ \frac{B_x}{E_x} &= \frac{-iD_s n_z}{c(S_s - n^2)}, \quad \frac{B_y}{E_x} = \frac{P_s n_z}{c(P_s - n_s^2)}, \quad \frac{B_z}{E_x} = \frac{iD_s n_x}{c(S_s - n^2)}, \end{aligned} \quad (8)$$

with refractive index components  $n_x$  and  $n_z$  transverse and parallel to  $\mathbf{B}_0$  given by

$$n_x = n \sin \theta_k, \quad n_z = n \cos \theta_k, \quad (9)$$

where the angle  $\theta_k$  of the  $\mathbf{k}$  vector (normal to planes of constant wave phase) measured with respect to  $\mathbf{B}_0$  is taken to be in the  $x$ - $z$  plane (Figure 1b). The squared

$$n^2 = \frac{B \pm \sqrt{(R_s L_s - P_s S_s)^2 \sin^4 \theta_k + 4 P_s^2 D_s^2 \cos^2 \theta_k}}{2A}, \quad (10)$$

with the sign on the radical chosen such that  $n^2 > 0$ , and with  $A$  and  $B$  given by

$$\begin{aligned} A &= S_s + (P_s - S_s) \cos^2 \theta_k, \\ B &= P_s S_s + R_s L_s + (P_s S_s - R_s L_s) \cos^2 \theta_k, \end{aligned}$$

where, for wave frequency  $\omega = 2\pi f$  and for  $k$  species of charge  $q_k$ , the Stix parameters are

$$\begin{aligned} S_s &= (R_s + L_s)/2, \quad D_s = (R_s - L_s)/2, \quad P_s = 1 - \sum_k \frac{\omega_{pk}^2}{\omega^2} \\ R_s &= 1 - \sum_k \frac{\omega_{pk}^2}{\omega^2} \left( \frac{\omega}{\omega + \omega_{hk}} \right), \quad L_s = 1 - \sum_k \frac{\omega_{pk}^2}{\omega^2} \left( \frac{\omega}{\omega - \omega_{hk}} \right) \end{aligned}$$

where  $\omega_{pk}^2 = N_k q_k^2 / \epsilon_0 m_k$ , and  $\omega_{hk} = q_k B^0 / m_k$ . From the ratios in (8) the magnitude of the time-averaged Poynting flux  $S^w = \langle |\mathbf{S}^w| \rangle$ , where  $\mathbf{S}^w = (1/2) \text{Re} \{ \mathbf{E}^w \times \mathbf{B}^w / \mu \}$ , may for convenience be related to the single reference component  $B_y^w$  as [Bell, 1984; Jasna *et al.*, 1993]

$$|B_y^w|^2 = \frac{2\mu_0}{c} S^w X^2 n \cos \theta_k \cdot \sqrt{(\tan \theta_k - \rho_1 \rho_2)^2 + (1 + \rho_2^2 X)^2}, \quad (11)$$

where  $X = P_s / (P_s - n^2 \sin^2 \theta_k)$  and

$$\rho_1 = \frac{E_z^w}{E_y^w} = \frac{(n^2 - S_s) n^2 \sin \theta_k \cos \theta_k}{D_s (n^2 \sin^2 \theta_k - P_s)}, \quad \rho_2 = \frac{E_x^w}{E_y^w} = \frac{n^2 - S_s}{D_s}.$$

Thus, for a specified cold plasma supporting oblique waves having wave normal angle  $\theta_k$  and wave power density  $S^w$ , the full wave field components required by (5) may be found from (11) and (8).

## 2. Oblique Whistler Model

### 2.1. Oblique Whistler Simulation

The required oblique whistler wave fields at any point are completely specified by the propagation delay or group time  $t_g$  (the variation of which gives the  $f$ - $t$  dispersion), the wave normal angle  $\theta_k$  and the wave power density  $S^w$ . In general these parameters vary with frequency and location throughout the magnetosphere and as such may be written  $t_g(\lambda, f, L)$ ,  $\theta_k(\lambda, f, L)$ , and  $S^w(\lambda, f, L)$ . As no closed-form expression for these wave properties exists, a comprehensive VLF ray tracing methodology is developed to determine these quantities after the pioneering efforts of *Edgar* [1976], as follows.

The propagation of whistler-mode electromagnetic waves in the magnetosphere is determined largely by the static Earth magnetic field and cold plasma density gradients. Here the Earth field is taken to be dipolar, and the cold background plasma density is assumed to be in a state of diffusive equilibrium along any par-

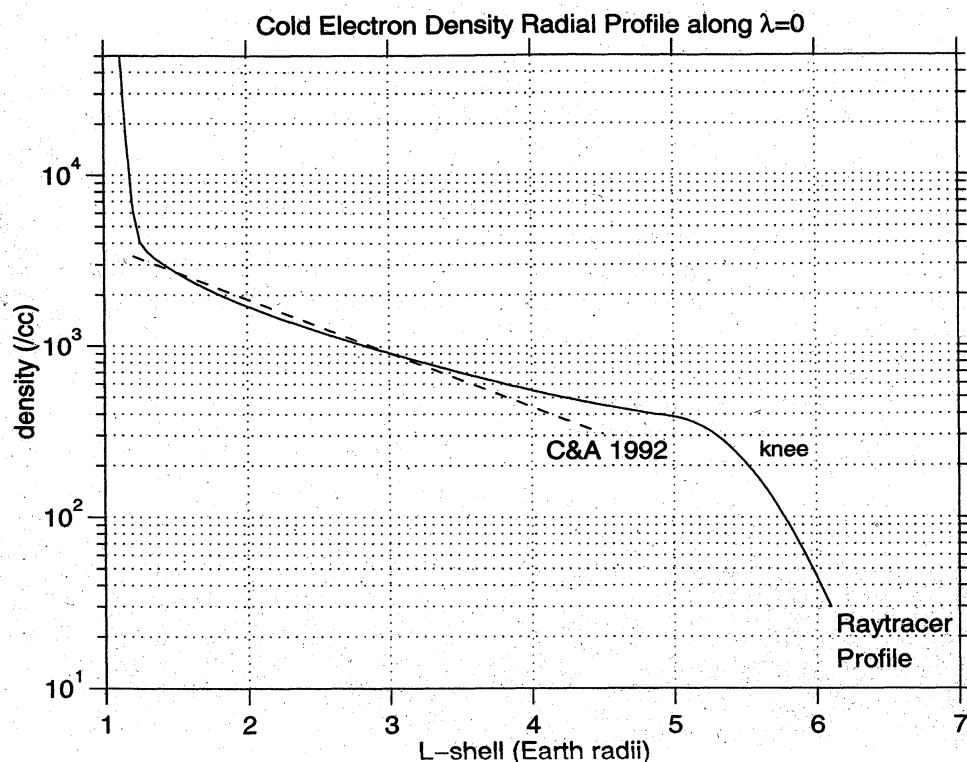


Figure 2. Assumed cold plasma equatorial density radial profile used for ray tracing.

ticular field line [Angerami and Thomas, 1964], and to vary smoothly throughout the magnetosphere. Figure 2 shows the assumed equatorial electron density profile set to match (approximately) the form  $\log_{10} N_{eq}(L) = -0.31L + 3.90$  (dashed-line) offered by Carpenter and Anderson [1992] for poststorm conditions, extending to a plasmopause “knee”  $L$  value [Carpenter et al., 1971] sufficiently high to permit the ray paths to reach  $L \geq 4$ .

Using the Stanford VLF ray tracing program [Inan and Bell, 1977], bundles of ray paths for each frequency  $f$  of a set spanning 200 Hz to 10 kHz are traced from the topside ionosphere throughout the magnetosphere, and the wave properties at the ensuing ray path/field line intersections are tabulated along selected  $L$  shells of interest over  $1.8 < L < 4.0$ . Plate 2 shows a representative ray bundle for the whistler packet midband frequency  $f=5$  kHz. Here rays are injected at altitude  $h_i = 1000$  km over the latitude range  $15^\circ < \lambda_i < 62^\circ$  with initial wave normal angles at the injection points taken as locally vertical, representing the mean value for the cone of wave normal angles transmitted through the horizontally stratified ionosphere [Helliwell, 1965]. Rays are traced over the first traverse through the magnetosphere until at the southernmost latitudes the wave normal angles become highly oblique, leading either to possible landau damping [Thorne, 1968; Sazhin, 1991] and/or total internal reflection within the magnetosphere (MR reflection) [Draganov et al., 1992; Ristic-Djurovic et al., 1998], depending on the prevailing hot plasma density distribution. For brevity, consideration

is limited herein to the primary effect induced by the first traverse of the whistler through the magnetosphere.

In Plate 2 the sequence of dashed lines transverse to the ray paths indicate wavefronts advancing at the ray group velocity, while the solid circles along  $L = 2.6$  indicate a representative set of ray/ $L$  shell intersection points at which the group propagation time and wave normals (short line segments rooted along  $L = 2.6$ ) are available directly. Here the particular ray paths to these intersection points are shown heavier for clarity. A rather fine injection latitude spacing of  $\Delta\lambda_i = 0.15^\circ$  and corresponding high spatial density of rays is necessary to ensure a sufficient number of ray path/ $L$  shell intersections in order to adequately sample the variation in wave properties along all  $L$  shells of interest. In the Southern Hemisphere the rays become naturally field-aligned for considerable distance so that the crossings become sparse; here the wave properties are interpolated from closest approach rays on either side of the field line.

Ray tracings are repeated at 200 Hz spacing for frequencies  $200 \text{ Hz} \leq f \leq 10 \text{ kHz}$ . As the frequency is changed the corresponding variation in refractive index value (10) alters the propagation delay and ray path curvature. This curvature variation warrants special attention as illustrated in Plate 3, which shows ray paths for two representative frequencies near the limits of the broadband whistler frequency range, namely  $f=1$  kHz and  $f=10$  kHz, plotted in two equivalent coordinate systems for clarity. Referring to Plate 3a, rays at higher

frequencies ( $f = 10$  kHz) generally exhibit tighter radius of curvature than those at lower frequencies ( $f = 1$  kHz), while rays at intermediate frequencies vary in a smooth manner between these representative limits.

An important consequence of this frequency-dependent curvature is that for any two distinct frequencies to reach the same point  $C = (L, \lambda)$ , as they must do in order to account for the coherent oblique whistlers actually observed [Lauben *et al.*, 1999], they must originate at different ionospheric injection latitudes as illustrated. Then even as the wave energy follows distinct paths to reach  $C$ , phase coherency is maintained throughout the whistler packet by virtue of the essentially simultaneous impulsive VLF wave excitation over all input latitudes and assumed smooth variation of the magnetosphere, considered on respective time and spatial scales set by the whistler mode.

While the group time  $t_g$  and wave normal angle  $\theta_k$  are available directly at the intersection points, the local wave power density  $S^w$  must be assessed from the combined effects of geometric ray-bundle defocusing and whistler-mode frequency-time dispersion determined by comparing rays launched at incremental latitudes and at successive frequencies. Accordingly, the wave power density is expressed as  $S^w = S_g^w S_d^w$ , where  $S_g^w$  is the geometric defocusing factor and  $S_d^w$  is the dispersion factor, and where  $S_g^w$  and  $S_d^w$  together vary in a way which conserves the total wave energy entering the magnetosphere. More specifically, the first factor  $S_g^w$  is associated with the change in wave power density transverse to the direction of power flow which occurs as the geometric cross-sectional area varies with increasing distance along the ray paths. This area varies in two dimensions as (1) the separation between a pair of rays emanating from adjacent launch points within the same meridional plane varies with position along the rays due to ray bundle defocusing (labeled as “width variation” in Plate 3a), and (2) the separation between two implied adjacent meridional planes containing mirror-image ray bundles at infinitesimal angular separation varies with distance from the Earth. Thus the cross-sectional area is defined by four rays in total (two in each mirror-image meridional plane), and  $S_g^w$  is estimated from the ratio in area at each ray/ $L$  shell intersection point to that at the ray launch points.

The second factor  $S_d^w$  is associated with the frequency dispersive nature of the medium which causes the electromagnetic energy of the whistler wave packet to become spread out in space along the direction of propagation with increasing distance along the ray paths. This effect is illustrated in Plate 3b by the two dark patches indicated by the two arrows which show the comparative length of a 1 kHz bandwidth pulse at both early ( $t=0.02$  s) and later ( $t=0.43$  s) times. This longitudinal spreading likewise reduces the local energy density in a manner independent from ray bundle defocusing. To conserve wave energy,  $S_d^w$  obeys the relation

$S_d^w = S_o^w [\partial t_g / \partial f]^{-1}$  (after Chang [1983]) where  $S_o^w$  is the reference input spectrum at the ray injecting points, and  $\partial t_g / \partial f$  is estimated numerically at each point from the variation in group time  $t_g(\lambda, f)$  between successive frequencies.

**2.1.1. Oblique whistler wave packet.** In general,  $t_g$ ,  $\theta_k$  and  $S^w$  are tabulated over frequency along  $L$  shells spaced at  $\Delta L = 0.2$  over the range  $1.8 \leq L \leq 4.0$ , and afterward interpolated onto a finely spaced uniform latitude grid with  $\Delta \lambda \leq 0.1^\circ$  required by the resonance scattering calculation. Plate 4 shows the resulting dynamic behavior and characteristic properties of the simulated whistler wave packet. Plate 4a (top left) shows wave packet snapshots at four selected times ( $t = 0.01, 0.15, 0.5$ , and  $1.5$  s) color-contoured at 1 kHz intervals. Note that in general the spatial extent of the packet grows at higher latitudes as the ray paths diverge and as dispersion causes the lower frequencies to lag behind the packet leading edge at later times. Note also the substantial increase in arrival time to the magnetic equator (and beyond) for higher  $L$  shells as compared with lower  $L$  shells, and how for later times (e.g.,  $t=1.5$  s) at high  $L$  shells (e.g.,  $L=4$ ) the leading edge is no longer defined by  $f=10$  kHz, consistent with the development of a whistler “nose” (i.e., the frequency of minimum delay, see Plate 4b for  $L=4, \lambda=0$ ), where this term, originally applied to ducted whistlers received on the ground [Helliwell, 1965] is here extended to the case of oblique whistlers within the magnetosphere. Plate 4b (top right) shows the dispersing whistler  $f$ - $t$  traces which are “observed” from the simulation at  $L = 2, 3$ , and  $4$  at magnetic latitudes  $\lambda = -20^\circ, 0^\circ$ , and  $20^\circ$  as the wave packet passes these fixed points. Note once again the large difference in arrival times over the range of  $L$  values, and the development of the whistler nose at frequencies  $f < 10$  kHz at higher latitudes for higher  $L$  shells.

Figures 4c, 4d, and 4e show wave field properties which develop along representative  $L = 2.0$ . Plate 4c shows the group time  $t_g$  over latitude  $\lambda$ , parametric in frequency  $f$ , which by comparison with the lower panel of Plate 4b for  $L=2$  can be seen to lead to these indicated  $f$ - $t$  traces. In like manner, Plate 4d shows the variation in effective wave power density normalized to  $1 \text{ W m}^{-2} \text{ Hz}^{-1}$  at the ray injection points. Note that the wave power decreases by  $\sim 30$  dB near the magnetic equator owing to the combined effects of  $S_g^w$  and  $S_d^w$ , increasing somewhat at locations south of the equator (more so at higher frequencies) from the reconverging ray paths (see Plate 2). This form and amount of wave power density variation is typical for most frequencies along most  $L$  shells. Finally, Plate 4e shows the variation in wave normal angle with  $\lambda$ , seen to vary nearly linearly with latitude and essentially identically for all frequencies except at the southernmost latitudes; this behavior is typical for all  $L$  shells, although the  $\theta_k(\lambda)$  slopes differ somewhat for each  $L$  shell.



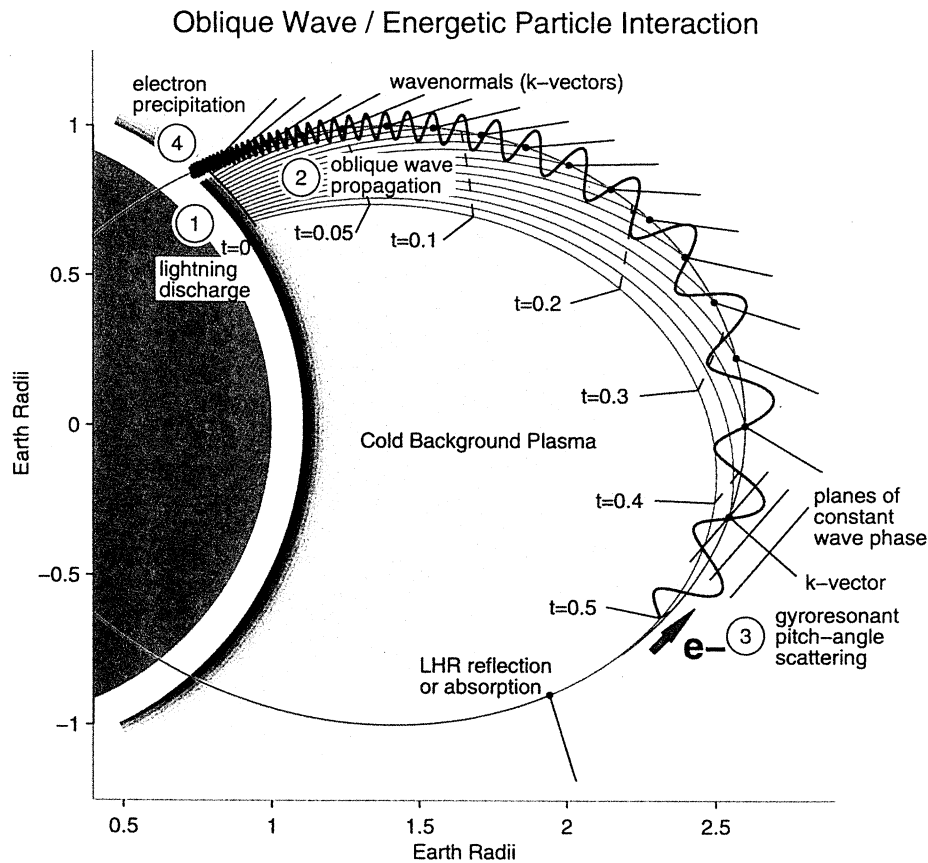


**Plate 1.** Lightning-induced electron precipitation (LEP) from oblique wave/energetic particle scattering along a particular magnetic field line. The lightning discharge leads to oblique mode propagation throughout the magnetosphere so that particles along field lines both inside and beyond the field line shown are also affected. The event sequence 1-4 is discussed in the text.

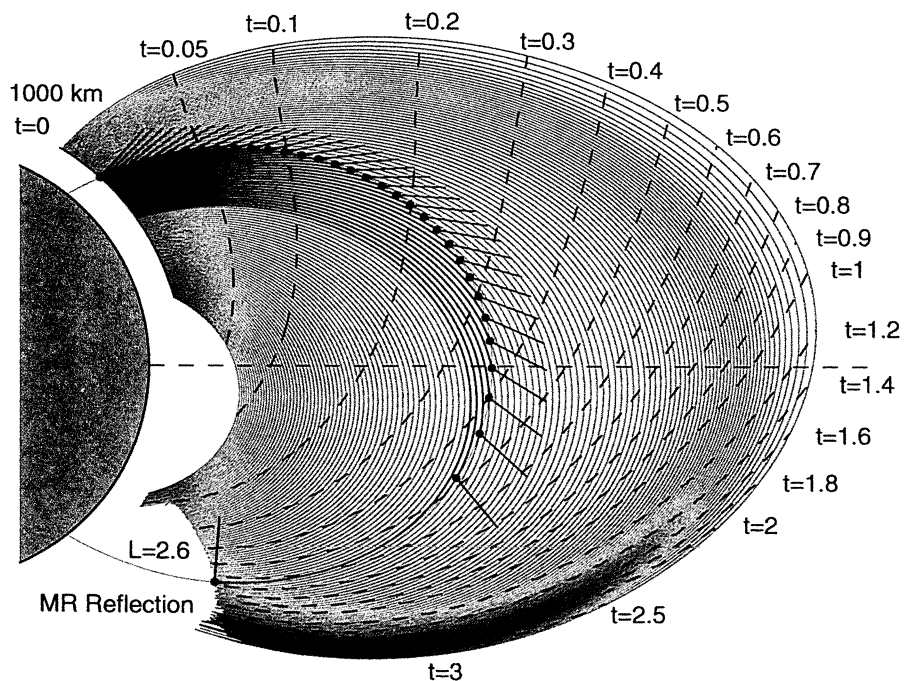


**Plate 2.** Representative oblique whistler-mode ray path bundle for  $f=5$  kHz. Dashed lines show wavefronts at the indicated group times; solid circles indicate ray/ $L$  shell intersections for (representative)  $L=2.6$ . Actual ray spatial density used is twice that shown. Propagation group times are in seconds.



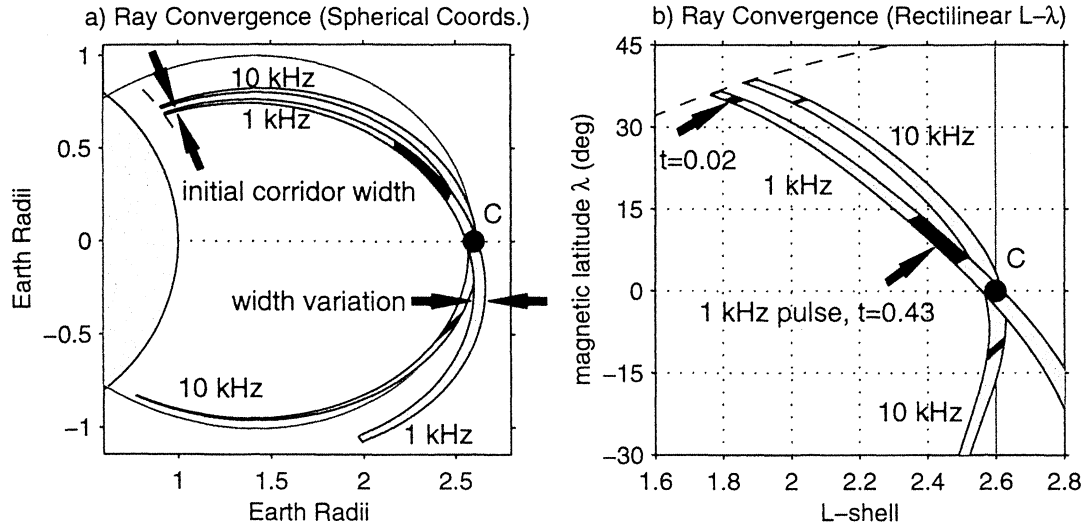


**Plate 3.** Ray convergence to a common point C from distinct injection latitudes for  $f=1$  kHz and  $f=10$  kHz rays, shown in both (a) geophysical and (b) rectilinear  $L$ - $\lambda$  coordinates. In general, rays at higher frequencies exhibit tighter radius of curvature as shown. The two sets of arrows in Plate 3a indicate the variation in separation between two adjacent  $f=1$  kHz (co-meridional) rays. The pair of arrows in Plate 3b indicate dark patches which depict pulse stretching due to  $f$ - $t$  dispersion for a 1 kHz bandwidth (exaggerated for clarity) at times  $t=0.02$  and  $0.43$  s. The much shorter pulses along the  $f=10$  kHz ray paths (the second beyond point C) in Plate 3b are for the same two times.

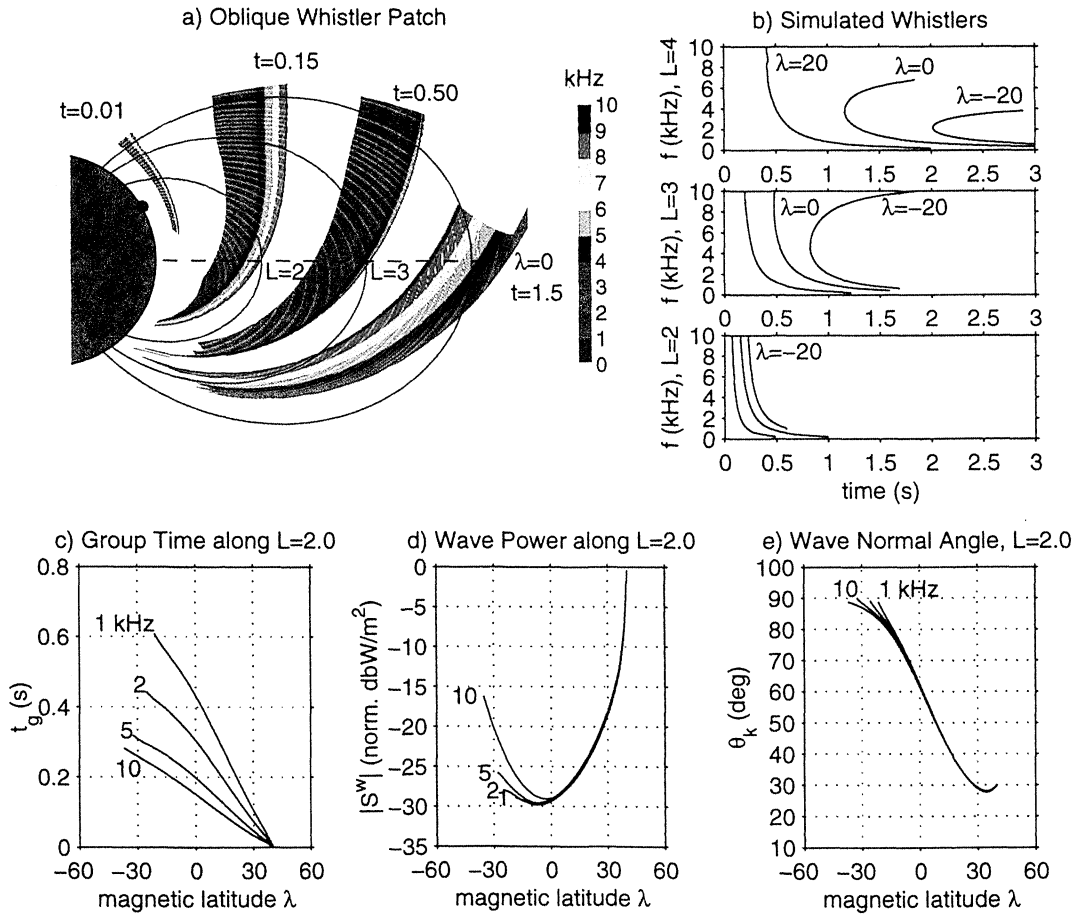


**Plate 4.** (a) Advancing broadband oblique wave packet at four successive locations, (b) Simulated whistler  $f$ - $t$  dispersion for  $L=2, 3, 4$  at  $\lambda=-20^\circ, 0^\circ, 20^\circ$ , and representative wave field properties (c) group time  $t_g$ , (d) normalized wave power  $S^w$ , and (e) wave normal angle  $\theta_k$  along  $L=2$ .

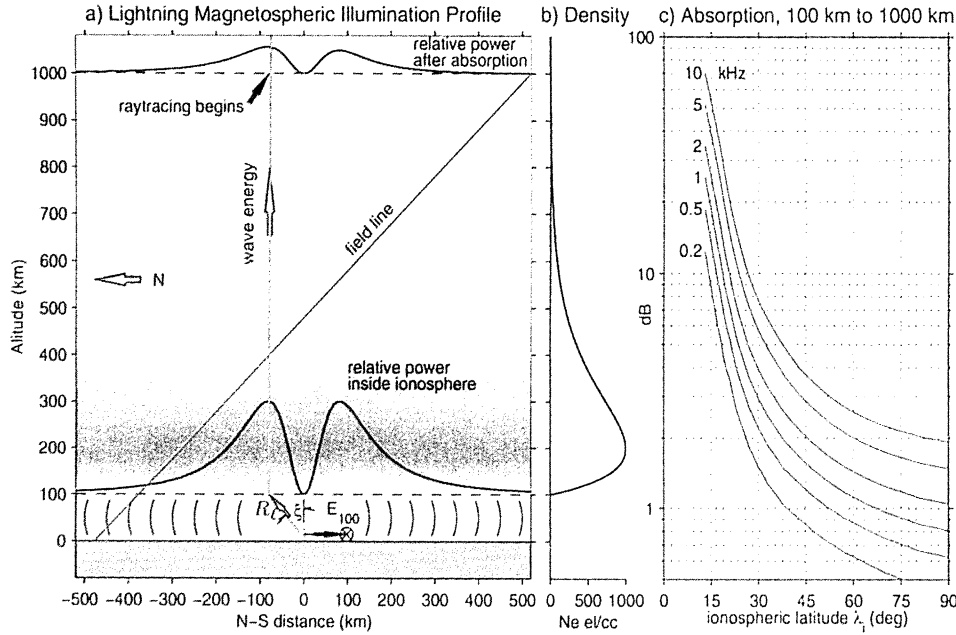


**Plate 5.** Lightning-magnetosphere VLF illumination model: (a) lightning source and wave illumination profiles along the ionosphere lower boundary (100 km) and reaching the magnetosphere (~1000 km) where ray tracing begins; (b) assumed ionospheric electron density profile; (c) wave power absorption through the ionosphere (quiet nighttime conditions).

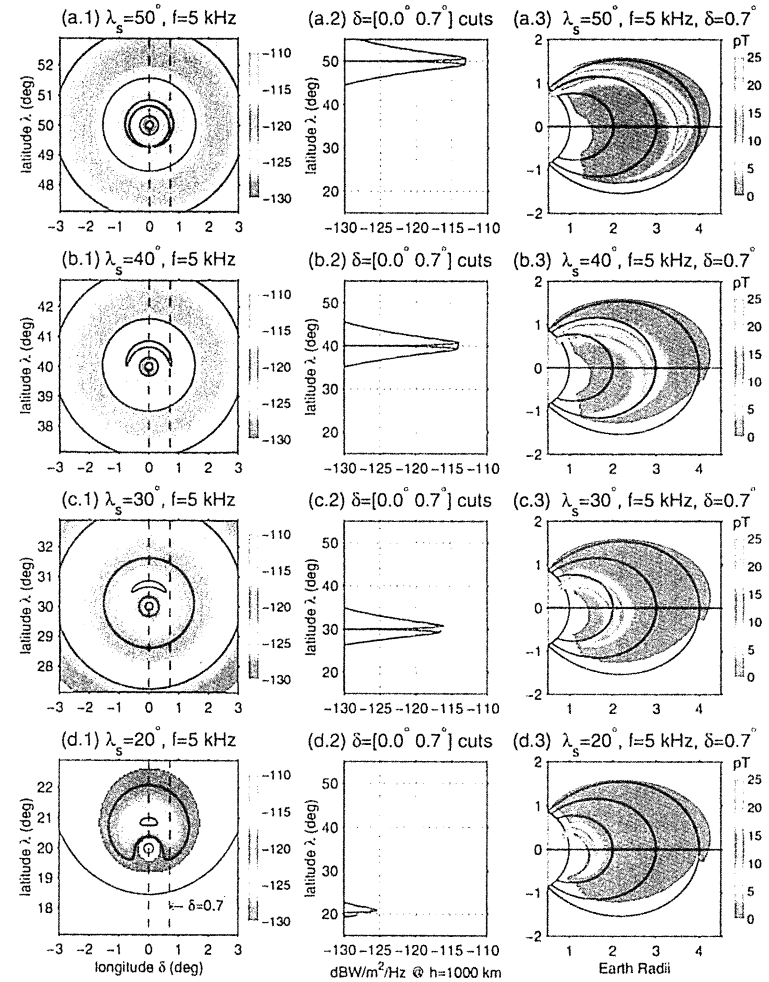


**Plate 6.** (left column) Lightning energy incident at  $h_i = 1000$  km where tracing starts after accounting for coupling loss and ionospheric absorption, for lightning at latitude  $\lambda_s = 20^\circ, 30^\circ, 40^\circ$ , and  $50^\circ$  (bottom to top), for model parameters given in the text. (center column) Wave power spectral density profiles versus latitude for the indicated slices along constant longitude. (right column) Whistler  $B_y^w$  component intensities for  $f=5$  kHz throughout the magnetosphere, after accounting for ray bundle defocusing and  $f$ - $t$  dispersion as determined by ray tracing, shown over all time. Equatorial intensities along the most strongly illuminated ray paths range ~10 to 30 pT.

## 2.2. Lightning-Magnetosphere Illumination Model

The whistler model developed thus far assumes a normalized wave input power spectral density of  $1 \text{ W m}^{-2} \text{ Hz}^{-1}$  at all ray injection points and for all frequencies. In order to accurately determine the latitude/longitude extent of the magnetospheric region over which significant scattering and precipitation occurs it is necessary to take into account the strong spatial dependence and nominal frequency dependence of the electromagnetic wave intensity radiated by a particular lightning discharge occurring at a specified location.

Plate 5 illustrates the approach and assumptions used to estimate the radiated wave spectral power density at magnetospheric altitude  $h_i = 1000 \text{ km}$  where ray tracing begins. Plate 5a shows the location within the Earth-ionosphere waveguide of the assumed lightning discharge (where  $R_\ell = 0$  corresponds to a given source geomagnetic latitude  $\lambda_s$ ) and the association between a representative point  $(R_\ell, \xi)$  at which wave energy enters the ionosphere at altitude  $h_p = 100 \text{ km}$  and the location at which the ray tracing wave input power is specified at  $h_i = 1000 \text{ km}$ . Then for a vertical cloud-to-ground lightning discharge, from the definition for current  $I = dQ/dt$  and lightning dipole moment  $M = 2h_e Q$ , where  $h_e$  is the height of the initial  $+Q$  charge above ground, the electric field at a distant point  $(R_\ell, \xi)$  is given by *Uman* [1984, p. 61]

$$E = \mu_o \frac{\sin \xi}{4\pi R_\ell} \left[ \frac{d^2 M}{dt^2} \right] = \mu_o \frac{\sin \xi}{4\pi R_\ell} (2h_e) \left[ \frac{dI}{dt} \right], \quad (12)$$

where  $R_\ell$  is the distance from lightning source to observation point,  $\xi$  is measured with respect to local vertical and where the brackets  $[\ ]$  denote evaluation with time delay  $t_o = R_\ell/c$ . Radiation at VLF frequencies can be modeled using the discharge current profile [after *Cummer and Inan*, 1997]

$$I(t) = I_o (e^{-bt} - e^{-at}), \quad (13)$$

giving radiated far-field time domain electric field  $E$  and power spectral density  $S(\omega)$

$$E = \mu_o \frac{\sin \xi}{4\pi R_\ell} (2h_e I_o) [a e^{-at} - b e^{-bt}], \quad (14)$$

$$S(\omega) = \frac{1}{Z_o} \left( \frac{\mu_o h_e I_o}{2\pi} \right)^2 \left( \frac{\sin \xi}{R_\ell} \right)^2 \frac{\omega^2 (a-b)^2}{(\omega^2 + a^2)(\omega^2 + b^2)}, \quad (15)$$

where  $Z_o = 377 \Omega$  is the impedance of free space and  $a$  and  $b$  are spectrum model parameters.

In general, the impulsive cloud-to-ground lightning discharge radiates electromagnetic wave energy in all directions within the Earth-ionosphere waveguide (Plate 5a) according to (15). However, since (15) is for unbounded radiation, the ideal factor  $1/R_\ell^2$  must be modified to account for additional subionospheric

attenuation due to absorption and wave mode interference. For the present work it is sufficient to adopt the approach of *Inan et al.* [1984], which notes from the multimode waveguide calculations of *Crory* [1961] that to first order the radiated power falls as  $1/R_\ell^2$  for  $100 \text{ km} < R_\ell \leq 1500 \text{ km}$  and  $2 \text{ dB}/1000 \text{ km}$  thereafter for  $R_\ell > 1500 \text{ km}$  (for points measured along the ground). Accordingly, the wave power density for points along the base of the ionosphere is taken to be that given by (15) but with the  $1/R_\ell^2$  factor modified to match the indicated power versus distance profile. Then since only a fraction of this power is directed vertically upward (especially at large  $R_\ell$ ), an additional factor  $\cos \xi$  is applied to (15) to conservatively estimate the available power flowing across the free-space/ionosphere boundary. A typical resulting pattern is shown in Plate 5a as the double-peaked profile situated at altitude  $h_b = 100 \text{ km}$  (relative scale). Then after accounting for coupling and polarization loss (3 dB) the wave energy is taken to propagate vertically from  $h = 100 \text{ km}$  to  $h_i = 1000 \text{ km}$  where ray tracing begins, suffering significant additional absorption along the way owing to collisional losses occurring primarily in the denser regions of the ionosphere ( $100 \leq h \leq 700 \text{ km}$ , Plate 5b) after the frequency- and latitude-dependent loss profiles taken from *Helliwell* [1965] and reproduced for reference in Plate 5c. A representative wave power profile at  $h_i = 1000 \text{ km}$  in the magnetosphere is shown in Plate 5a (using the same relative scale as the profile at  $h_b = 100 \text{ km}$ ) which matches low-altitude satellite overflight measurements of ground-based VLF transmitter signals [*Crory*, 1961; *Rastani et al.*, 1985]. Finally, lightning discharge current parameters  $a = 5 \times 10^3$ ,  $b = 1 \times 10^5$  are selected to give a typical spectrum broadly-peaked between  $f = 2$  and  $f = 6 \text{ kHz}$ , and stroke height  $h_e = 5 \text{ km}$  and reference current  $|I_o| = 10.53 \text{ kA}$  are adopted to give rather strong but not uncommon whistler intensity values  $B_y^w \sim 10$  to  $30 \text{ pT}$  at points along the magnetic equator matching in situ measurements [*Lauben*, 1998; *Lauben et al.*, 1999].

## 2.3. Complete Oblique Whistler Model

The lightning illumination model is evaluated for the set of source latitudes  $\lambda_s = 20^\circ, 30^\circ, 40^\circ$ , and  $50^\circ$ , and applied as input to the normalized whistler model of the previous section. Plate 6 shows column-wise from left to right (1) lightning magnetospheric illumination contours for representative midband frequency  $f = 5 \text{ kHz}$  at the injection altitude  $h_i = 1000 \text{ km}$  as seen from overhead the lightning source, (2) power spectral density profiles versus latitude for both central and slightly off-center longitudinal meridians (to avoid the dipole pattern null) indicated by the dashed vertical lines in the adjacent contour plots, and (3) the resulting whistler  $B_y^w$  wave field spatial intensity patterns evaluated throughout the magnetosphere (from (11)) in the off-center meridional plane, for all time. Each

lightning source is seen to lead to a maximum wave intensity in the range  $\sim 10$  to  $30$  pT for some point along the magnetic equator at an  $L$  shell higher than that of the source. These wave magnetic field intensities with the  $f$ - $t$  forms and wave normal angles of Plate 4 are well representative of a fundamental class of oblique whistlers commonly observed in the magnetosphere [Lauben, 1998; Lauben *et al.*, 1999].

### 3. Precipitation Signatures

#### 3.1. Scattering Calculation

The scattering calculation procedure is similar to that of *Chang and Inan* [1985]; here a concise overview will suffice. Referring to Plate 7a, as the wave propagates from northern to southern latitudes (Plate 4), at each of a succession of wavefront encounter latitudes  $\lambda_{\text{wf}}$  along a given  $L$  shell of interest, a distribution of northward streaming energetic electrons (1 keV up to 3 MeV in general, but tailored to each  $\lambda_{\text{wf}}$  and  $L$ ) having pitch angles initially at the edge of the loss cone enters the advancing wave packet. The test particles subsequently undergo gyroresonance scattering at locations  $\lambda_{\text{res}} \geq \lambda_{\text{wf}}$  for which the resonance condition (7) is satisfied specific to each particle's local parallel velocity  $v_{\parallel}$ . The wave fields which prevail along each test particle trajectory are determined by first noting the time of initial wavefront encounter  $t_{\text{wf}} = t_g(\lambda_{\text{wf}}, f_{\text{wf}}^{\ell})$  defined by the group time required for the leading frequency  $f_{\text{wf}}^{\ell}$  to arrive at  $\lambda_{\text{wf}}$  (see Plate 4b), and thereafter accumulating the particle transit time  $t_p(\lambda)$  associated with the particle advance through the wave packet to track the overall total laboratory time  $t_{\text{lab}}(\lambda) = t_{\text{wf}} + t_p(\lambda)$  at each integration step. Knowledge of  $t_{\text{lab}}(\lambda)$  at each step prescribes the instantaneous frequency  $f(\lambda) < f_{\text{wf}}^{\ell}$  seen by the particle whose group time matches the lab time  $t_g(\lambda, f) = t_{\text{lab}}(\lambda)$ , and this knowledge of  $(\lambda, f)$  in turn selects the corresponding wave normal angle  $\theta_k(\lambda, f)$  and wave power density  $S^w(\lambda, f)$  at that point in space and time.

Each value of initial parallel velocity  $v_{\parallel o}$  spanning the range of resonant energies at resolution  $\Delta v_{\parallel o} = 0.1 \times 10^6$  m/s is applied to a constellation of twelve test particles all having initial loss cone pitch angles  $\alpha_{\text{eq}}^i = \alpha_{\text{eq}}^{\text{lc}}$  (from (4)) distributed uniformly over initial relative wave-particle gyrophase  $\eta_o$  between the particle velocity and wave  $\mathbf{B}_{\text{R}}^w$  vectors (Equation (5c) and Figure 1c), since the specific value of  $\eta_o$  determines whether a given particle is scattered to ultimately greater or lesser pitch angle. As the equations of motion are integrated over latitude  $\lambda$  each particle takes a unique trajectory in velocity-gyrophase space  $\{v_{\parallel}, v_{\perp}, \eta\}_{\eta_o}$  indexed to  $\eta_o$ , and at the point of exit from the wave the final pitch angles  $\alpha^f = \tan^{-1} v_{\perp}/v_{\parallel}$  are calculated and adiabatically mapped to corresponding equatorial reference values  $\alpha_{\text{eq}}^f$ . These  $\alpha_{\text{eq}}^f$  are subtracted from the assumed initial  $\alpha_{\text{eq}}^i = \alpha_{\text{eq}}^{\text{lc}}$  value to obtain the

set of pitch angle deviations  $\Delta\alpha_{\text{eq}}(v_{\parallel o}, \eta_o)$  over initial velocity  $v_{\parallel o}$  and gyrophase  $\eta_o$ , where the set of final scattered pitch angles  $\alpha_{\text{eq}}^f$  may thus be recovered from  $\alpha_{\text{eq}}^f(v_{\parallel o}, \eta_o) = \alpha_{\text{eq}}^i + \Delta\alpha_{\text{eq}}(v_{\parallel o}, \eta_o)$ . In general, roughly half the particles are scattered to larger pitch angles ( $\Delta\alpha_{\text{eq}} > 0$ ) and half to smaller pitch angles ( $\Delta\alpha_{\text{eq}} < 0$ ) the latter with correspondingly lower mirror altitudes.

It necessary to also account for those particles not initially at the edge of the loss cone which are nonetheless scattered to some angle  $\alpha_{\text{eq}}^f < \alpha_{\text{eq}}^{\text{lc}}$  within the loss cone. As it turns out, the set of deviations  $\Delta\alpha_{\text{eq}}(v_{\parallel o}, \eta_o)$  remain essentially unchanged as the initial pitch angle  $\alpha_{\text{eq}}^i$  is varied even up to several degrees to either side of the loss cone; thus the one set  $\Delta\alpha_{\text{eq}}(v_{\parallel o}, \eta_o)$  may be applied to the remaining  $\alpha_{\text{eq}}^i$  over the range  $\alpha_{\text{eq}}^{\text{lc}} < \alpha_{\text{eq}}^i \leq (\alpha_{\text{eq}}^{\text{lc}} + \max|\Delta\alpha_{\text{eq}}|)$  to efficiently complete the calculation. The full set of test particle deflections is then convolved with an assumed ambient energetic electron phase space density  $f_v^i(v_{\parallel}, \alpha_{\text{eq}})$  scaled to give reference flux  $j_o = 1 \times 10^8$  el cm $^{-2}$  s $^{-1}$  keV $^{-1}$  at  $E=1$  keV having velocity dependence  $f_v \sim 1/v^6$  (after *Inan et al.*, [1982], *Ristic-Djurovic et al.* [1998]) and taken as initially void for  $\alpha_{\text{eq}} < \alpha_{\text{eq}}^{\text{lc}}$  (Plate 7b), to determine the perturbed phase space density  $f_v^p(v_{\parallel}, \alpha_{\text{eq}})$ , which generally becomes non-void for  $\alpha_{\text{eq}} < \alpha_{\text{eq}}^{\text{lc}}$  (Plate 7c). This perturbed  $f_v^p(v_{\parallel}, \alpha_{\text{eq}})$  is then converted to an equivalent flux distribution function  $j(E, \alpha_{\text{eq}})$  suitable for subsequent calculations [Chang and Inan, 1985b], with mapping  $(v_{\parallel}, \alpha_{\text{eq}}) \rightarrow (E, \alpha_{\text{eq}})$  after *Ristic-Djurovic et al.* [1998].

This procedure is repeated for wavefront latitudes  $\lambda_{\text{wf}}$  over the range  $-36.5^\circ \leq \lambda_{\text{wf}} \leq 32.5^\circ$  at spacing  $\Delta\lambda_{\text{wf}} = 1^\circ$ , and the resulting set of wavefront-indexed flux distribution functions  $j_{\text{wf}}(E, \alpha_{\text{eq}})$  are integrated over the loss cone ( $0 \leq \alpha_{\text{eq}} \leq \alpha_{\text{eq}}^{\text{lc}}$ ), adjusting for solid angle and magnetic flux tube convergence [Ristic-Djurovic *et al.*, 1998] for the  $L$  shell dependent precipitation latitude  $\lambda_p$  given by

$$\cos^2 \lambda_p = (R_e + h_p)/(L R_e), \quad (16)$$

where  $h_p$  is the assumed precipitation altitude, and then combined to give the precipitation flux signature  $\Phi(E, t)$  at the foot of each  $L$  shell (Plate 7d) according to

$$\Phi(E, t) = 2\pi \frac{\sqrt{1 + 3 \sin^2 \lambda_p}}{\cos^6 \lambda_p} \cdot \sum_{\lambda_{\text{wf}}} \int j_{\text{wf}}(E, \alpha) \cos \alpha \sin \alpha d\alpha, \quad (17)$$

where the summation  $\sum$  indicates the superposition of the consecutive wavefront-indexed precipitation energy-time ( $E$ - $t$ ) profiles which develop as each  $j_{\text{wf}}(E, \alpha)$  is adjusted for the energy-dependent particle transit time required to reach  $\lambda_p$  from each  $\lambda_{\text{wf}}$  [Inan *et al.*, 1982]. Finally, the number of precipitating electrons  $N(t)$  and

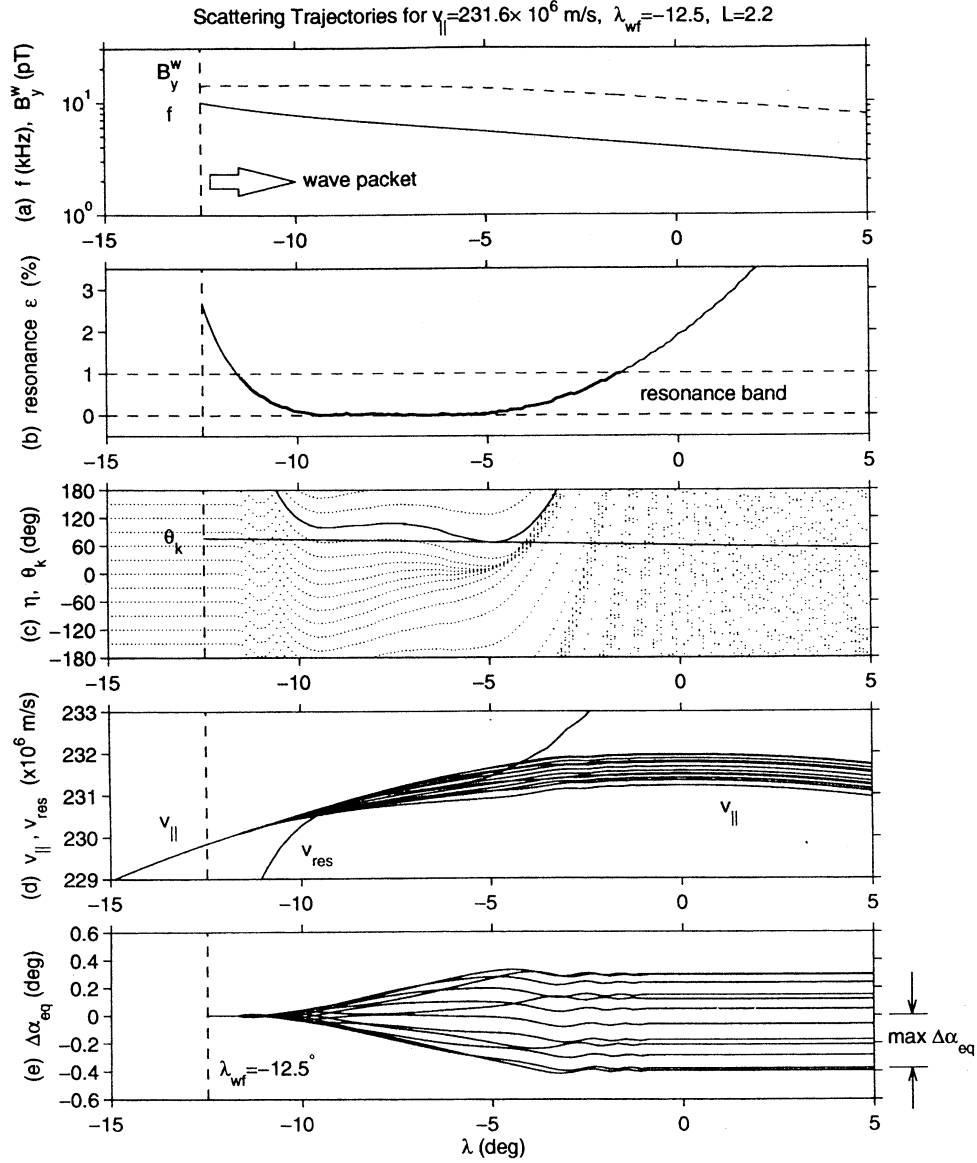


**Figure 3.** Typical oblique resonance and scattering trajectories (top down): (a) frequency  $f$  (kHz) and wave intensity  $B_y^w$  (pT) (on common log scale) seen by a particle moving along  $L = 2.2$  with initial equatorial velocity  $v_{||,eq} = 231.6 \times 10^6$  m/s and entering the wave packet at  $\lambda_{wf} = -12.5^\circ$ , (b) resonance parameter  $\epsilon = (v_{||} - v_{res})/v_{res}$  with 1% resonance band shown, (c) wave-particle relative gyrophase  $\eta$  (dotted, with one trajectory shown solid over the latitude range of strongest interaction) for twelve test particles sharing  $v_{||,eq}$ , distributed uniformly over initial phase  $\eta_o$ , also, wave normal angle  $\theta_k$  (solid), (d) resonance velocity  $v_{res}$  and scattered particle parallel velocity  $v_{||}(\lambda, \eta_o)$  for these twelve particles, (e) resulting  $\Delta\alpha_{eq}(\lambda, \eta_o)$  scattering trajectories; with  $\max |\Delta\alpha_{eq}|$  over  $\eta_o$  indicated.

the associated energy flux  $Q(t)$  which they represent are found by integrating  $\Phi(E, t)$  over energy

$$N(t) = \int_{E > E_{th}} \Phi(E, t) dE \quad (18)$$

$$Q(t) = \int_{E > E_{th}} E \Phi(E, t) dE \quad (19)$$

where a lower limit of integration  $E_{th}$  is introduced to explore the energy dependence of these results and to facilitate comparison with particle detector measure-

ments made above some given minimum energy sensitivity threshold.

**3.1.1. Scattering trajectories** Figure 3 shows the set of scattering trajectories  $\{v_{||}, v_{\perp}, \eta\}_{\eta_o}$  for a representative case of twelve test particles sampling  $\eta_o$  having  $v_{||,eq}^* = 2.316 \times 10^8$  m s<sup>-1</sup>, traveling northward along  $L = 2.2$ , and entering the whistler wave packet at  $\lambda_{wf}^* = -12.5^\circ$  (Plate 7a). Figure 3a (top panel) shows, on a common log scale, the frequency (solid line) and wave magnetic field  $B_y^w$  component intensity (dashed line) seen by these 12 particles. Here the

wave intensity ranges  $\sim 16$  to  $\sim 8$  pT as the frequency falls from  $f=10$  kHz to 300 Hz (and lower for  $\lambda > 5^\circ$ ). Figure 3b shows the value of the resonance parameter  $\epsilon = |(v_{\parallel} - v_{\text{res}})/v_{\text{res}}|$  with a 1% resonance band indicated (appropriate for this velocity). Figure 3c shows, on a common scale, the wave normal angle  $\theta_k \sim 60^\circ$  (solid) and the 12 gyrophase  $\eta(\lambda, \eta_o)$  trajectories (dotted), initially uniform over  $\pm 180^\circ$  (i.e., for  $\lambda < 12.5^\circ$ ) and subsequently altered during resonance, with one trajectory shown solid over the range of latitudes for which  $\eta$  remains within a  $\sim \pi/2$  band, representing a particularly extended solution to (6) for which the cumulative scattering is maximized. Figure 3d shows the twelve parallel particle velocity trajectories  $v_{\parallel}$  perturbed from their otherwise adiabatic values during resonance, as well as the  $v_{\text{res}}$  curve from (7) corresponding to  $\lambda_{\text{wf}} = -12.5^\circ$ . Last, Figure 3e shows the resulting pitch angle devi-

ations  $\Delta\alpha_{\text{eq}}(\lambda, \eta_o)$  from the otherwise constant equatorial loss cone value  $\alpha_{\text{eq}}^{\text{lc}} = 14.28^\circ$ . The peak absolute deviation  $\max|\Delta\alpha_{\text{eq}}|$  (over  $\eta_o$ ) is indicated at the right-side end of this panel, where for the present case, those particles most scattered have been deflected by  $\max|\Delta\alpha_{\text{eq}}| \simeq 0.4^\circ$  into the loss cone. This  $(v_{\parallel}^*, \lambda_{\text{wf}}^*)$  pair happens to be that combination for which the wave-particle interaction length is maximized, thus leading to the maximum peak  $|\Delta\alpha_{\text{eq}}|$  deflection for any set of particles traveling along this  $L$  shell.

Since for the conditions considered herein particles are scattered predominantly via momentum deflection induced by the wave magnetic field (versus acceleration by the wave electric field), and since in addition no prolonged particle Larmor-phase bunching occurs (as would indicate opportunity for reradiated coherent waves), no significant wave-particle energy exchange

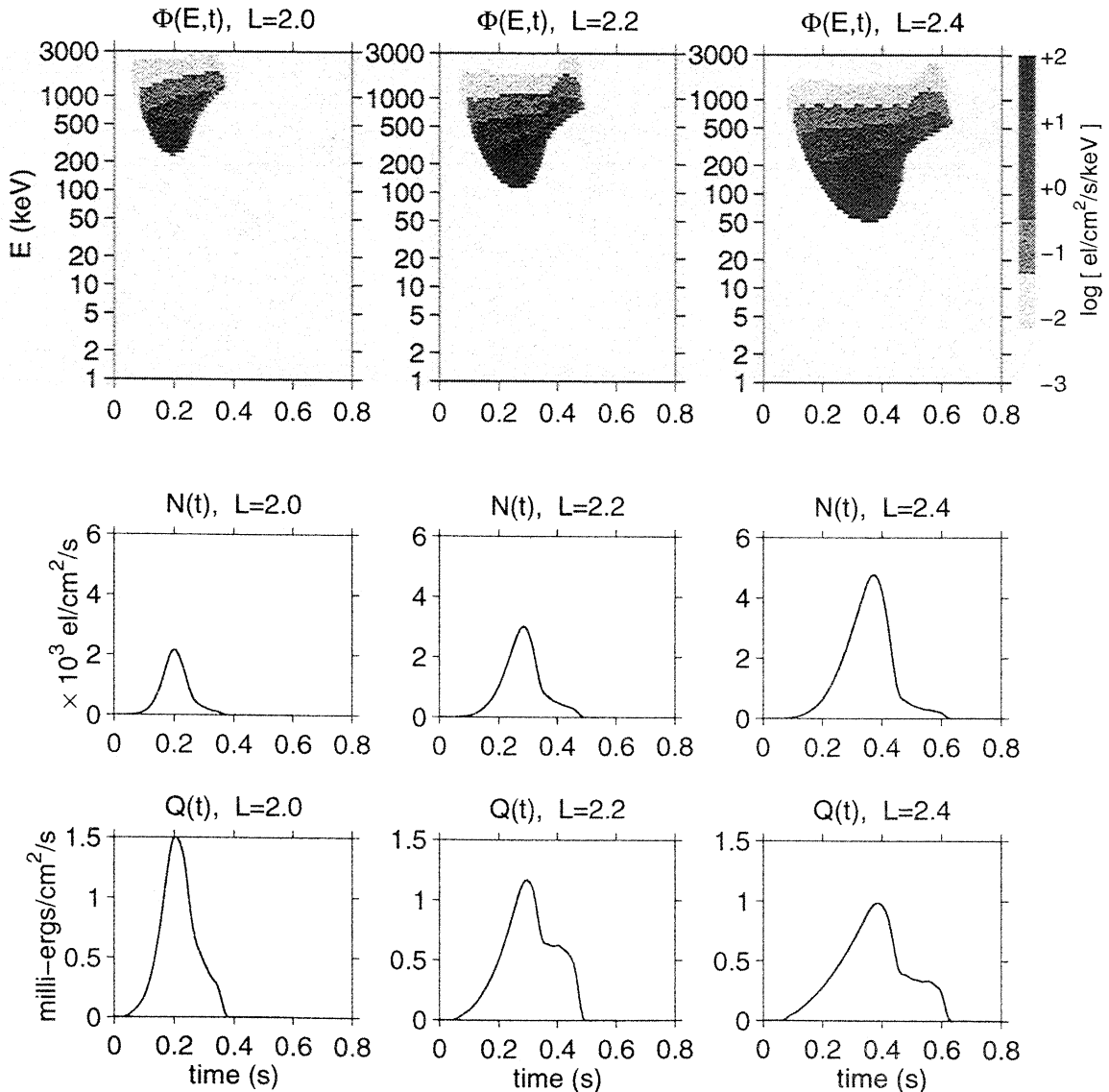


**Figure 4.** Precipitation signatures for  $\lambda_s = 30^\circ$  at the foot of three  $L$  shells sampling the region of maximum wave intensity (Plate 6c.3). Top to bottom: loss cone differential flux  $\Phi(E, t)$ , total electron flux  $N(t)$  and total energy flux  $Q(t)$  deposited to the upper atmosphere.

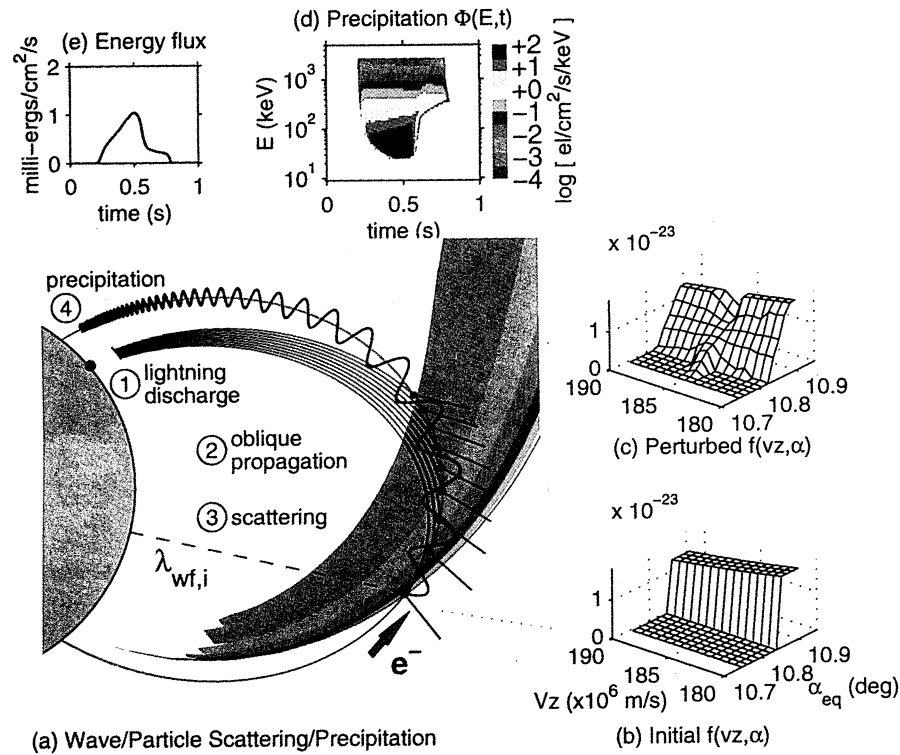


**Plate 7.** Formulation detail for a representative  $L$  shell. Counterclockwise from lower left: (a) Basic event sequence: (1) lightning discharge, (2) oblique whistler propagation, (3) gyroresonance scattering, (4) precipitation. (b) Initial energetic electron flux distribution entering the wave packet for this  $\lambda_{wf}$ , having initially void loss cone, (c) Perturbed flux distribution after gyroresonance interactions with the wave showing scattering into the loss cone, (d) Precipitation flux signature  $\Phi(E, t)$  for loss cone particles from all  $\lambda_{wf}$  along this  $L$ , (e) Precipitation energy flux pulse  $Q(t)$  deposited to the upper atmosphere.

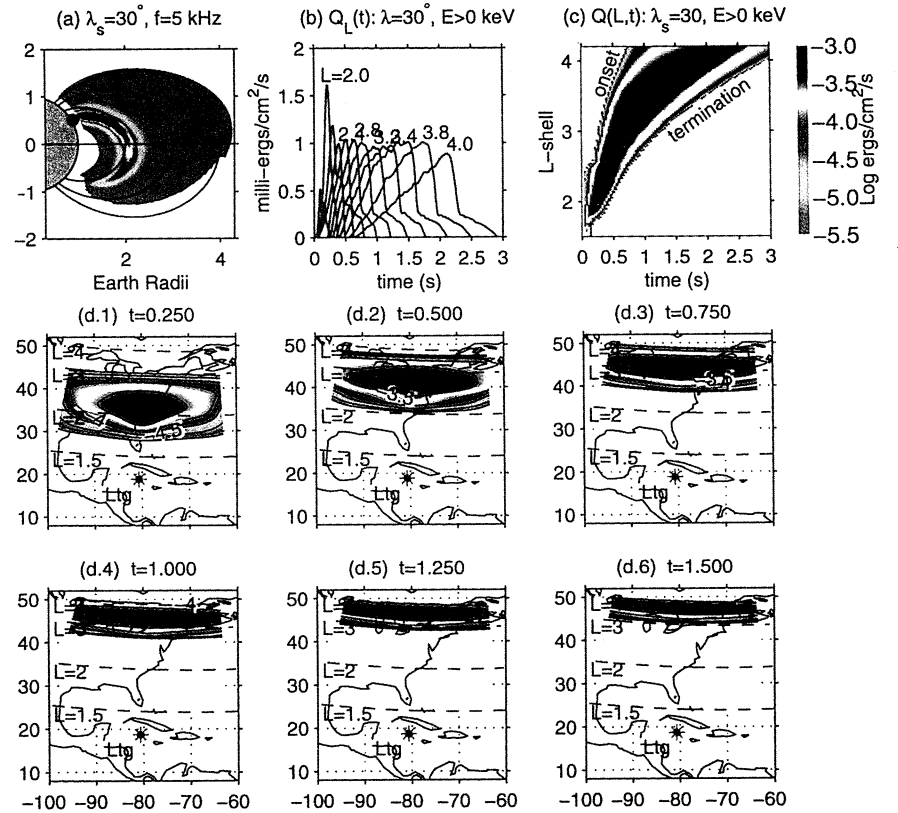


**Plate 8.** Precipitation hotspot sequence for  $\lambda_s = 30^\circ, E > 0$ . Explanation of panels given in text.



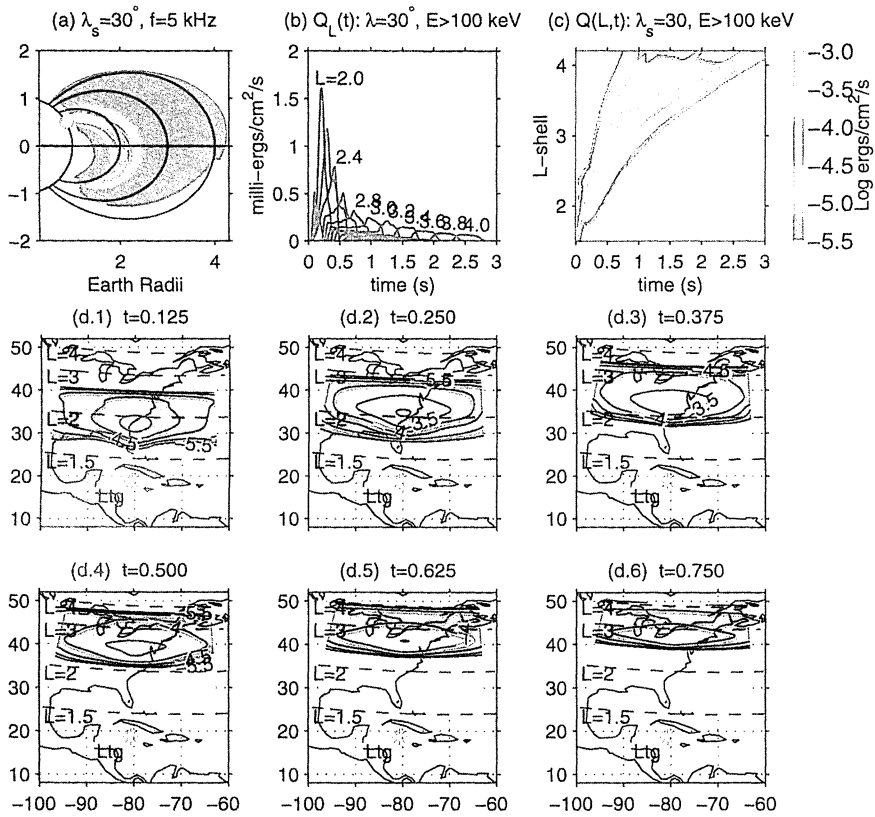


**Plate 9.** Precipitation hotspot sequence for  $\lambda_s = 30^\circ$ ,  $E > 100$  keV. Format same as previous figure.

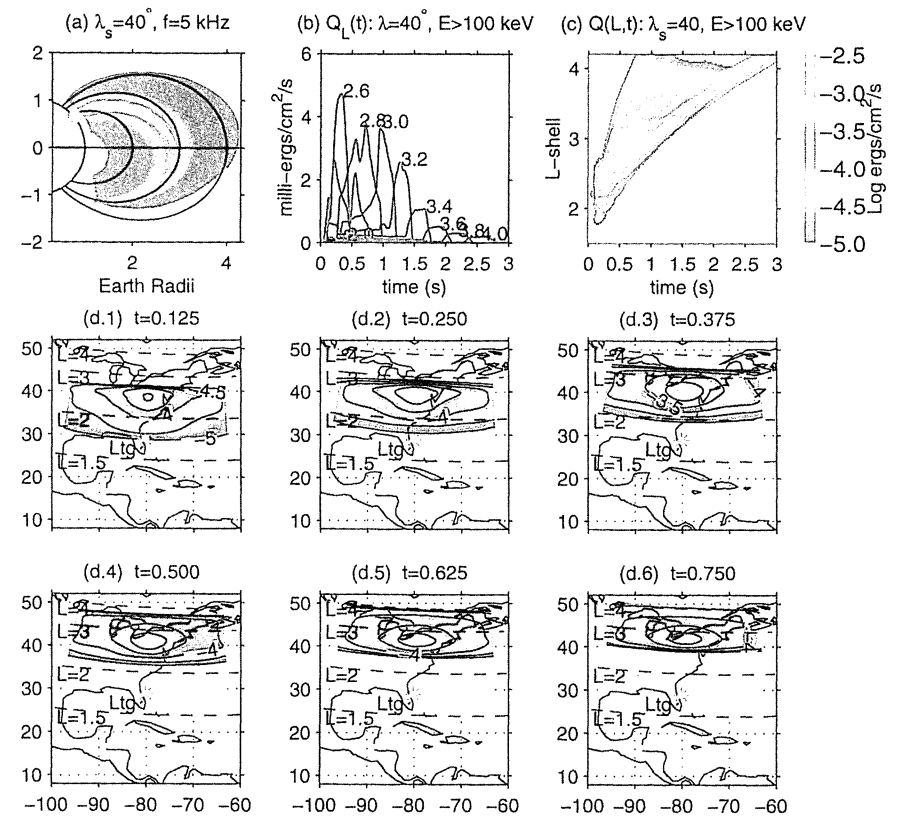


**Plate 10.** Precipitation hotspot sequence for  $\lambda_s = 40^\circ$ ,  $E > 100$  keV. Format same as previous figure.

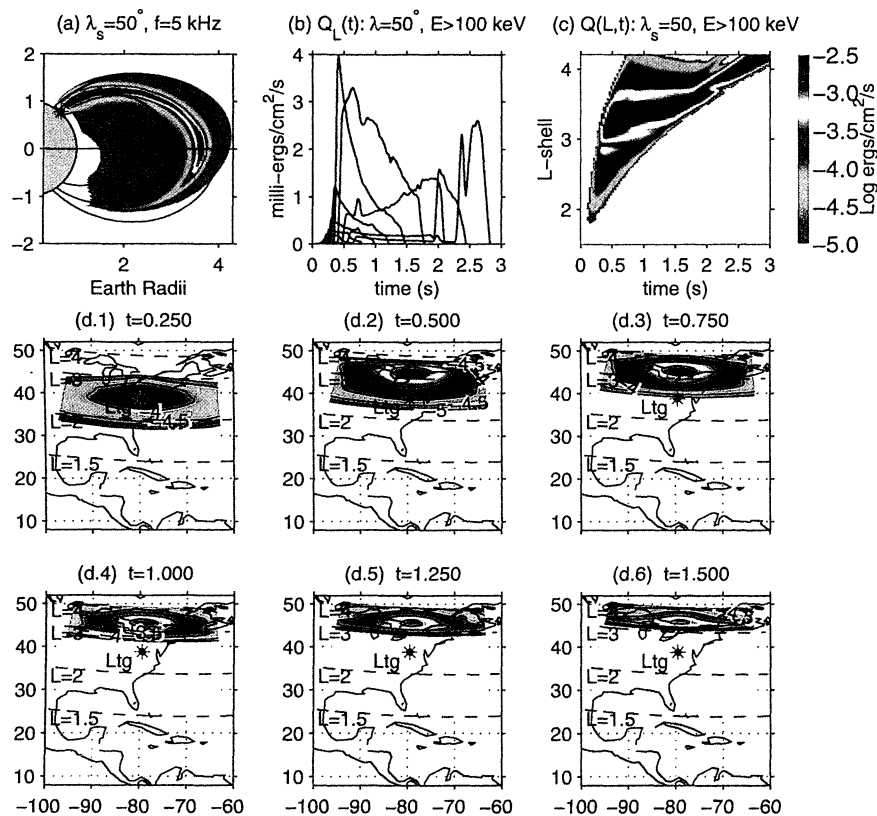


**Plate 11.** Precipitation hotspot sequence for  $\lambda_s = 50^\circ$ ,  $E > 100$  keV. Format same as previous figure.

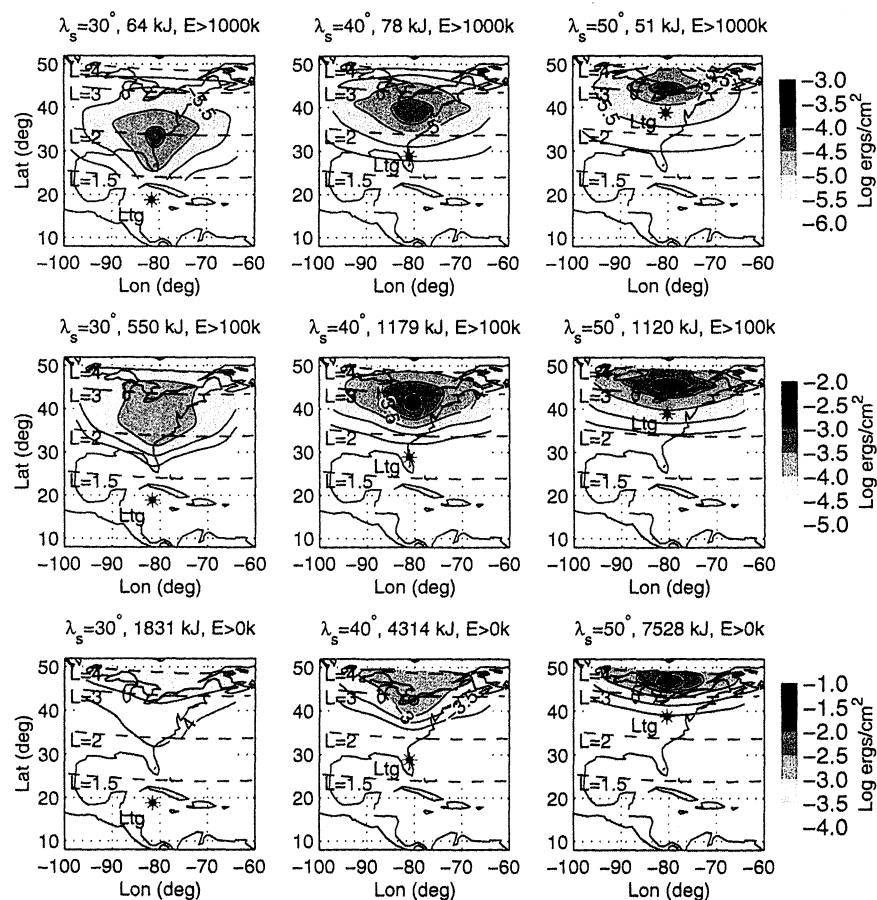


**Plate 12.** Precipitation fluence spatial density for  $E > 0$ ,  $E > 100$  keV, and  $E > \text{MeV}$  (bottom to top), for lightning located at  $\lambda_s = 30^\circ$ ,  $40^\circ$ , and  $50^\circ$  (left to right).

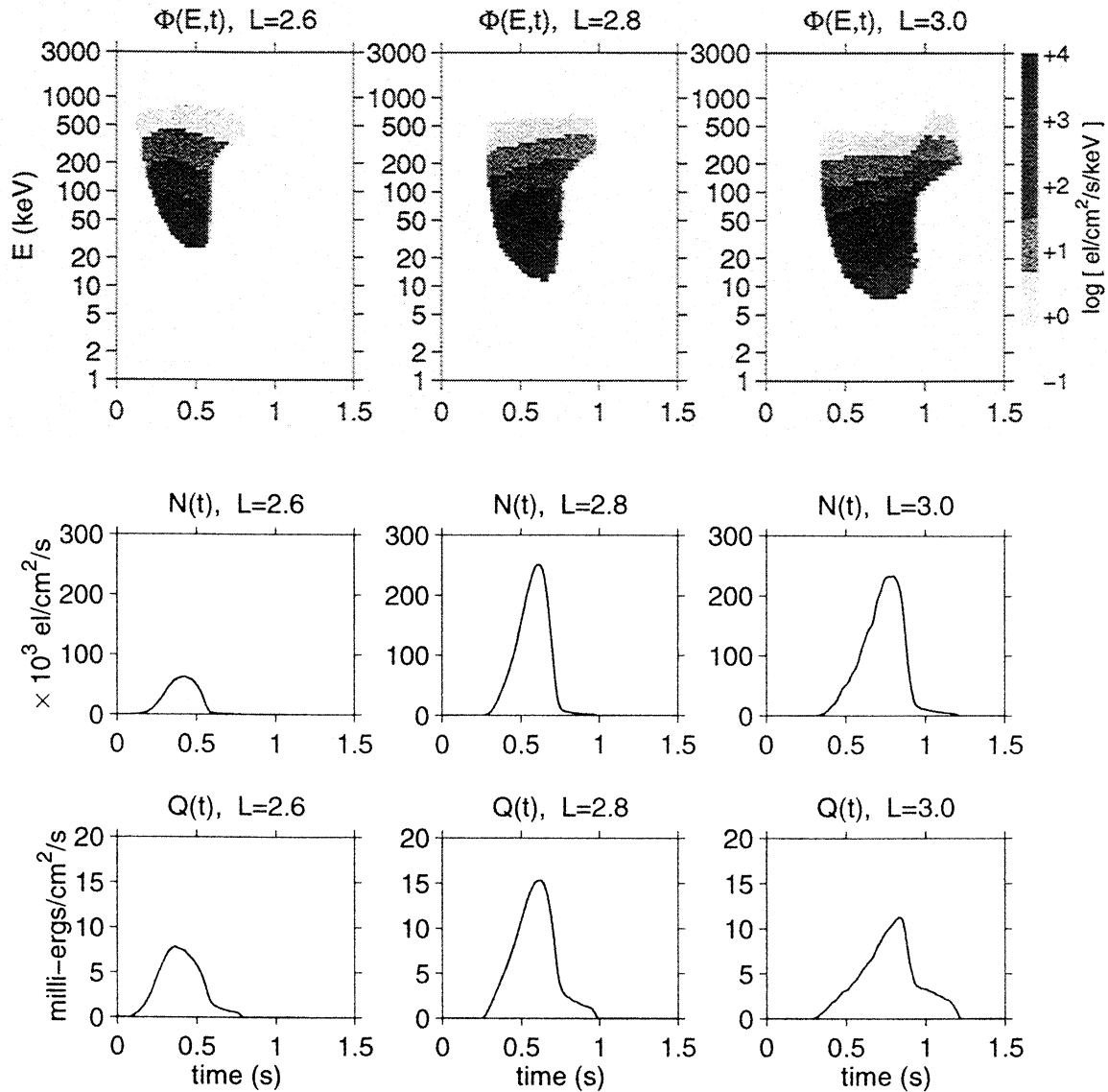


**Figure 5.** Precipitation signatures for  $\lambda_s = 40^\circ$  at the foot of four  $L$  shells sampling the region of maximum wave intensity (Plate 6b.3). Format same as for previous figure.

takes place and to first order, the waves are neither amplified nor damped during the interaction. This decoupling permits the whistler intensities to be established a priori and applied without subsequent adjustment.

### 3.2. Precipitation Signature Case Studies

Precipitation signatures for several cases are presented here. It is of interest to explore the manner in which the precipitation signatures vary depending on the particular “cut” made by a field line through the spatially varying whistler intensity patterns shown in the right most columns of Plate 6. The three figures show the variation in signatures for respective sets of three adjacent  $L$  shells ( $\Delta L = 0.2$ ) straddling the most intense ray paths illuminated by lightning at latitudes  $\lambda_s = 30^\circ$ ,  $40^\circ$ , and  $50^\circ$ .

**3.2.1. Lightning source at  $\lambda_s = 30^\circ$ .** Figure 4 shows the case for a lightning source at magnetic latitude  $\lambda_s = 30^\circ$ . The top row shows differential electron flux  $\Phi(E, t)$ , the second row, electron number flux  $N(t)$  and the lower row, precipitation energy flux  $Q(t)$ , for  $L = 2.0, 2.2$ , and  $2.4$ . Note that in this case although the maximum electron *number* flux  $N(t)$  occurs for  $L = 2.4$ , the maximum energy flux  $Q(t)$  actually occurs for  $L = 2.0$  since the generally higher resonant energies of these scattered particles for  $L = 2.0$  offset for their reduced number flux. This contrast stresses the significance of the assumed spectral hardness ( $f_v \sim 1/v^6$ ) in computing  $\Phi(E, t)$ ,  $N(t)$ , and  $Q(t)$  from  $\Delta\alpha_{eq}$ .

**3.2.2. Lightning source at  $\lambda_s = 40^\circ$ .** Figure 5 shows the case for  $\lambda_s = 40^\circ$ . Here the effective energy-time slope of the constant  $\Phi(E, t)$  flux contours (i.e.,

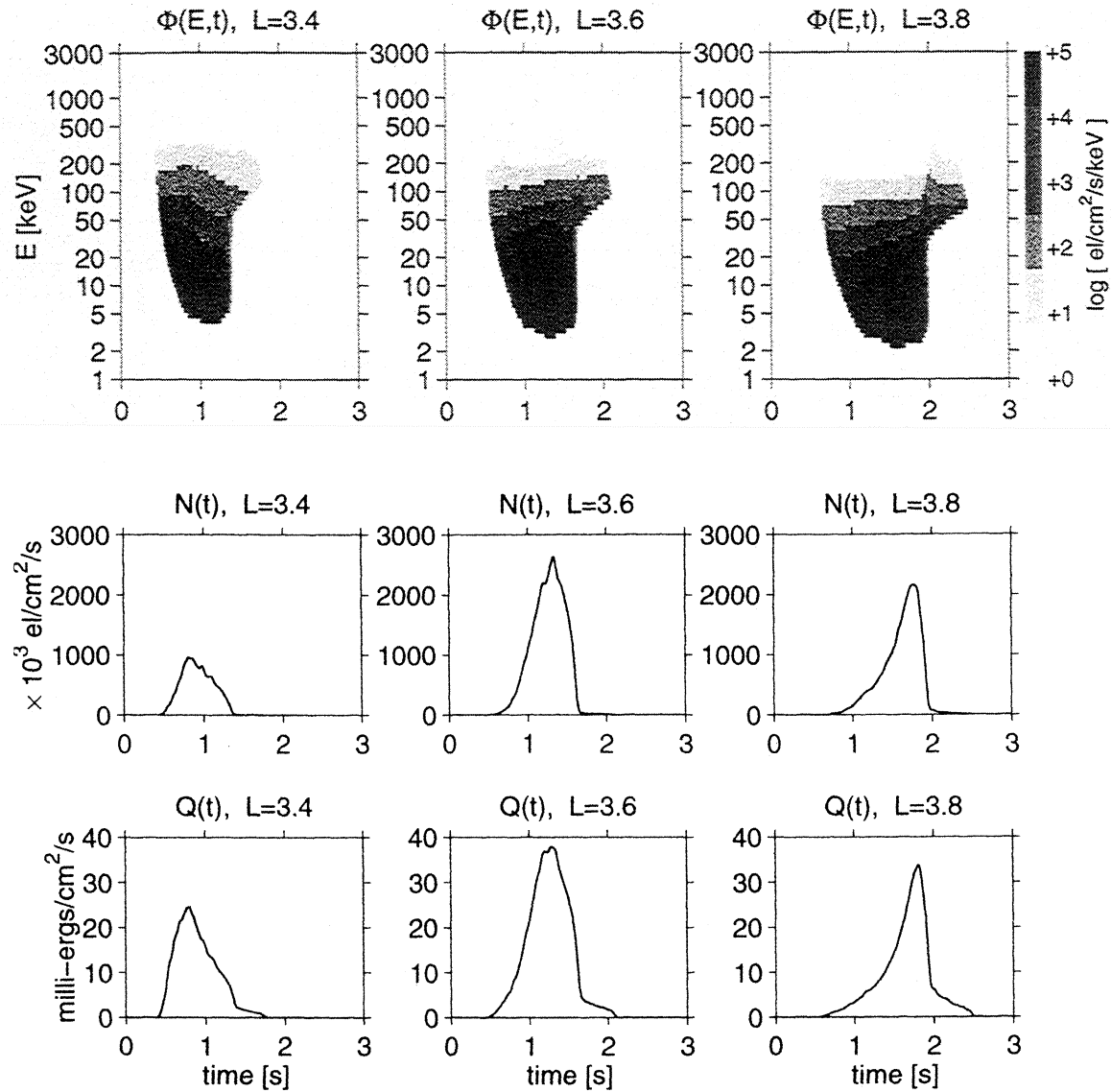


**Figure 6.** Precipitation signatures for  $\lambda_s = 50^\circ$  at the foot of four  $L$  shells sampling the region of maximum wave intensity (Plate 6a.3). Format same as for previous figure.

upper edges of the constant grey-level regions) varies in a systematic manner depending on whether the maximum wave intensities are encountered relatively close to, or far from, the lightning source. Specifically, with reference to the  $L$  shell having maximum equatorial wave intensity ( $L \sim 2.8$  at the representative frequency  $f = 5$  kHz, Plate 6b.3), at higher  $L$  shells the strong wave intensities south of the magnetic equator combine with the longer interaction lengths along these higher field lines (which expressed in degrees of latitude  $\lambda$  hold roughly constant), to the effect that particles arriving relatively late after the lightning discharge are those most strongly deflected, giving upward sloping contours in the  $\Phi(E, t)$  signatures (e.g., for  $L = 3.0$ ). Conversely, at lower  $L$  shells the strongest wave intensities are encountered closer to the lightning source with the result that particles arriving relatively soon after

the discharge are those most strongly deflected, giving downward sloping contours (e.g., for  $L = 2.6$ ). This systematic slope variation occurs over sufficiently separated  $L$  shells for any lightning source, as a direct result of the cross- $L$  propagation of the ray paths.

**3.2.3. Lightning source at  $\lambda_s = 50^\circ$ .** Figure 6 shows the case for  $\lambda_s = 50^\circ$ . Note the tremendous flux of  $\sim 10$  keV electrons (exceeding  $1 \times 10^5$  el  $\text{cm}^{-2} \text{s}^{-1}$ ) precipitated over  $3.4 \leq L \leq 3.8$  (and also outside this range) in response to this high-latitude lightning discharge. Note that the peak energy fluxes are on the order of several tens of milli-ergs  $\text{cm}^{-2} \text{s}^{-1}$ , comparable to weak auroral fluxes, albeit persisting for only a short time after the discharge. These flux levels are especially intense due to the combination of very long interaction lengths, higher available flux, and reduced momenta of the generally lower resonant energy (and

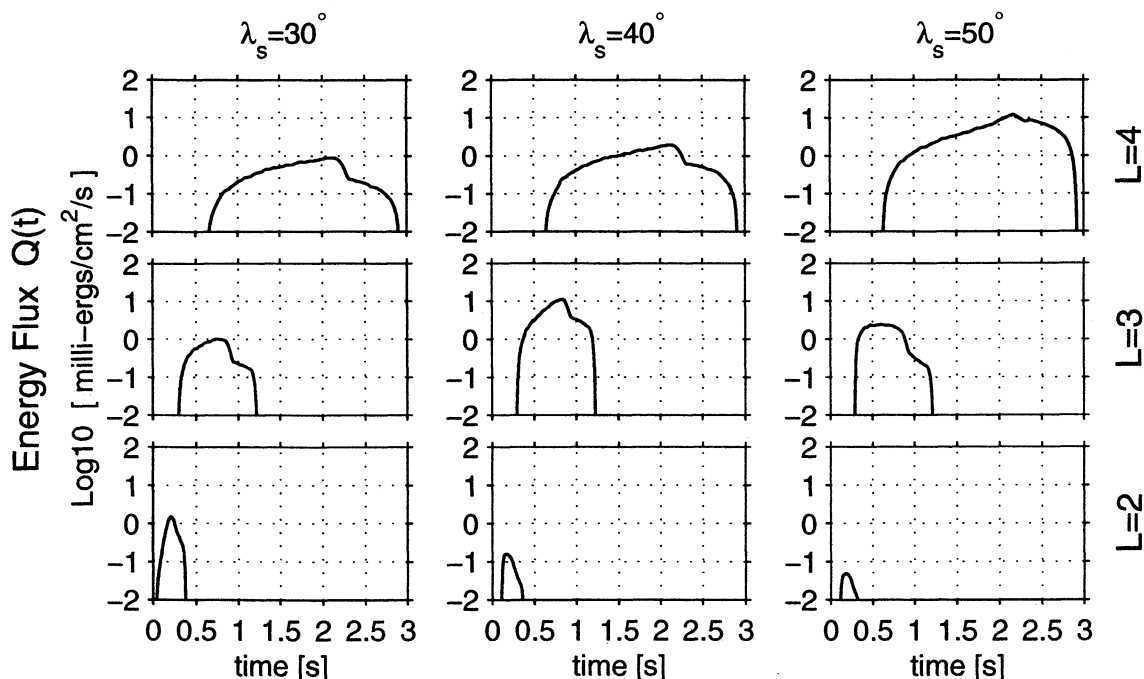


**Figure 7.** Comparative precipitation energy flux pulses at  $L=2$ , 3, and 4 (bottom to top) for  $\lambda_s=30^\circ$ ,  $40^\circ$  and  $50^\circ$  (left to right).

thus more readily deflected) particles at these high  $L$  shells, since the peak whistler intensities are essentially no greater than those which occur for other lightning source latitudes. This result suggests that of all factors considered, the variation in linear interaction length with  $L$  value may well be the most dominant in determining which  $L$  shells are most affected on average for a typical global-average distribution of lightning sources covering many tens of degrees of latitude.

**3.2.4. Summary over  $L$  and  $\lambda_s$ .** Figure 7 presents  $Q(t)$  signatures at the foot of  $L=2$ , 3, and 4 (bottom to top rows) for lightning locations  $\lambda_s = 30^\circ$ ,  $40^\circ$ , and  $50^\circ$  (left to right columns) on common log scales for direct comparison. Note that the arrival of the precipitation pulse for lower  $L$  shells always precedes that for higher  $L$  shells. This earlier arrival at low  $L$  shells is due to both the shorter propagation paths for the wave and the faster velocities of the generally higher resonant energy particles. Conversely, the later arrival at high  $L$  shells is due to the longer wave paths and slower velocities of the generally lower resonant energy particles. Note also the regularity in precipitation onset delay for each  $L$  shell. These pulse timing relationships are independent of lightning source latitude since for any interaction region, the wave propagation time and resonant particles energies are governed by the assumed (common) cold plasma properties; as such they reflect the state of the magnetosphere.

In contrast, the pulse intensity variation versus  $L$  shell (or equivalently, versus precipitation latitude) directly reflects the lightning source latitude in accord with the respective whistler spatial intensity patterns

of Plate 6. That is, at  $L = 2$  the energy flux is greatest for  $\lambda_s = 30^\circ$ , at  $L = 3$  the flux is greatest for  $\lambda_s = 40^\circ$  and at  $L = 4$ , for  $\lambda_s = 50^\circ$ , consistent with the equatorial crossings of most intensely illuminated ray paths. For  $\lambda_s=30^\circ$  the peak flux at all three  $L$  shells is nearly equal despite the reduced whistler intensities for  $L > \sim 2.5$  due to the increased linear interaction lengths and greater abundance of generally lower resonant energy (and thus more easily deflected) particles at high  $L$  shells. These factors, intrinsic to wave-particle gyroresonance in a dipole magnetic field for such typical prevailing energetic electron spectra, combine to promote generally enhanced scattering efficiencies and greater flux at higher  $L$  shells for equivalent wave intensities at respective  $L$ -adjusted resonant frequencies. For  $\lambda_s = 30^\circ$  these factors just balance the decreasing wave intensities to maintain nearly constant peak flux over all  $L$  shells, while for  $\lambda_s > 30^\circ$  these factors reinforce the peak wave intensities to give greatly increased flux for higher  $L$  shells.

## 4. Precipitation Hotspots

### 4.1. Hotspot Dynamic Behavior

In the previous section the precipitation energy-time signatures  $\Phi(E, t)$  and associated energy flux profiles  $Q(t)$  were calculated for selected  $L$  shells contained in a single magnetic meridian. Here consideration is extended over a range of magnetic meridians displaced up to several tens of degrees in longitude from that of the lightning source to determine the extent and behavior of the two-dimensional dynamic precipitation footprints

or “hotspots” which develop over extensive ionospheric regions. As a practical matter, the energy flux  $Q$  is first calculated for a fixed set of  $L$  shells and longitude displacements  $\delta$  (cf. Plate 6) and subsequently interpolated to form the quantity  $Q(\lambda_p, \delta, t)$ , where the triple  $(\lambda_p, \delta, t)$  denotes evaluation of the energy flux over essentially continuous values for magnetic latitude, longitude and time, and where (16) is employed to map  $L \rightarrow \lambda_p$ . For convenience in the discussion to follow,  $Q(\lambda_p, \delta, t)$  is referred to equivalently as  $Q(L, \delta, t)$  by this same mapping.

The next four figures each present three reference plots along the top row and a succession of two-dimensional spatial slices through  $Q(\lambda_p, \delta, t)$  taken at fixed time steps and projected onto geographic coordinates using a simple tilted-dipole mapping (sufficient for illustration purposes). These slices show precipitation hotspot development over space and time, and in particular their substantial displacement poleward relative to the location of the causative lightning discharge. Results are shown for several lightning source latitudes and lower energy limits  $E_{th}$  used in (19).

#### 4.1.1. Lightning source at $\lambda_s = 30^\circ$ , all energies.

Plate 8a (top left) repeats for reference the magnetospheric whistler wave intensity pattern of Plate 6c.3. Plate 8b (top center) shows an overlay of the individual precipitation energy flux profiles  $Q(L, \delta = 0, t)$  of the type shown in Figure 7 evaluated for selected  $L$  shells spanning  $1.8 \leq L \leq 4.0$  in the central meridian. In this case the highest peak flux occurs at  $L = 2.0$  due to the particularly intense wave fields along this  $L$  shell in conjunction with the general trend towards higher resonant energies at these lower  $L$  shells. This particular case exhibits the quite remarkable property that for  $L > 2.0$  nearly all  $Q(L, \delta = 0, t)$  flux profiles have the same peak value of 1 milli-erg  $\text{cm}^{-2} \text{s}^{-1}$ ; specifically, this result indicates that the greater numbers of predominantly lower energy electrons at higher  $L$  shells deposits the same peak energy flux as does the lesser flux of predominantly higher energy electrons at lower  $L$  shells (exclusive of  $L = 2.0$ ), again further emphasizing the importance of the much longer interaction lengths at higher  $L$  shells which compensate for the reduced wave intensities at those locations.

Plate 8c (top right) replots the profiles of Plate 8b with energy flux taking a color value, and  $L$  shell oriented along the  $y$  axis. Here the contour boundaries for flux onset, flux peak, and flux termination all manifest smoothly sloping forms over time, consistent with the trend shown earlier in Figure 7. In particular, the red-colored peak flux contour defined by (somewhat arbitrary)  $Q > 10^{-3.5} \simeq 0.32$  milli-erg  $\text{cm}^{-2} \text{s}^{-1}$  begins at the point  $t \sim 0.1$  s,  $L \sim 1.8$  and exhibits an initially linearly sloping  $L$ - $t$  onset edge which expressed in form  $t_p(L)$  behaves as  $dt_p/dL \sim 0.25$  up to  $t \sim 0.5$  s,  $L \sim 3.5$ , breaking to a gentler arch thereafter up to  $t \sim 1.2$  s,  $L = 4$ , where the flux persists at this level for duration

$\sim 1.2$  s. This well-defined behavior suggests that observation of such smooth, continuous  $t_p(L)$  spread over many  $L$  (or equivalently,  $t_p(\lambda_p)$  spread over many degrees of latitude) for individual LEP events constitutes a robust, readily testable criteria for oblique-mode precipitation which is not sensitive to the particular lightning discharge characteristics nor specific energetic electron spectral hardness.

Considering the precipitation flux onset versus time profiles of Plate 8c simultaneously incident upon the upper atmosphere over a continuum of latitudes, the resulting precipitation burst appears first at low latitudes and moves rapidly poleward with time. To clearly illustrate this effect, Plates 8d.1 through 8d.8 (lower two rows) show the spatiotemporal development of the precipitation flux hotspots  $Q(\lambda_p, \delta, n\Delta t)$  at time steps  $\Delta t = 1/4$  s, projected onto geographic latitude and longitude coordinates over the eastern United States (using the same energy flux scale as Plate 8c). Note that the mapping from magnetic dipole coordinates to geographic coordinates has the effect of subtracting  $\sim 11^\circ$  (the approximate dipole axis tilt) from the lightning magnetic latitude for the chosen longitude ( $\sim 80^\circ$  W), so that this source at  $\lambda_s = 30^\circ$  appears at a geographic latitude of  $\sim 19^\circ$ . A more precise mapping using an IGRF model subtracts an additional  $\sim 1.5^\circ$  latitude at these longitudes [Johnson et al., 1999].

The first time frame (Plate 8d.1) at  $t = 1/4$  s represents the earliest arrival of significant energy flux ( $\sim 1$  milli-erg  $\text{cm}^{-2} \text{s}^{-1}$ ). At its widest points the hotspot size for this flux level already extends  $\sim 20^\circ$  in longitude and  $\sim 8^\circ$  in latitude, and is centered at  $L \sim 2.2$  or  $\sim 36^\circ$  geographic latitude, or some  $17^\circ$  poleward of the causative lightning discharge. As mentioned previously, this poleward displacement arises from the cross- $L$  shell propagation of the oblique whistler waves from injection latitude to the magnetic equator (Plate 8a) where the strongest scattering takes place [Lauben, 1998]. By the next frame (Plate 8d.2) at  $t = 1/2$  s the hotspot center has moved further poleward to  $\sim 41^\circ$ , and has increased in longitudinal width to nearly  $30^\circ$ . The subsequent frames (Plates 8d.3-8d.8) show that significant levels of flux continue to precipitate for up to  $t = 3$  s, finally forming a thin band near  $50^\circ$  geographic latitude having width at least as wide as the extrapolation limit of  $36^\circ$  used here.

#### 4.1.2. Lightning Source at $\lambda_s = 30^\circ$ , energies $E > 100$ keV.

Since significant transient perturbations to the lower ionosphere (especially at altitudes  $< 90$  km accessible to measurement using VLF remote sensing techniques [Inan et al., 1990]) are thought to be caused primarily by energetic electrons in the range  $E \geq 100$  keV, it is of special interest to isolate the flux-time behavior of just these higher energies in a manner which is not obscured by the otherwise tremendous flux of precipitating lower energy electrons, which although substantial do not penetrate to low altitudes

to cause significant secondary ionization [Inan *et al.*, 1985a]. Accordingly, Plate 9 shows hotspot time slices for this same  $\lambda_s = 30^\circ$  lightning source but for energies  $E > 100$  keV ( $E_{th} = 100$  keV in (19)) and at shorter time steps  $\Delta t = 1/8$  s. Here at time  $t = 1/8$  s (Plate 9d.1) the most intense region of the spot first appears below  $L = 2.0$ , or some  $\sim 14^\circ$  poleward of the source, passing  $L = 2.2$  at  $t = 1/4$  s and just reaching  $L \sim 2.6$  by  $t = 1/2$  s, or equivalently  $\sim 42^\circ$  geographic latitude, notably less than the previous maximum latitude of  $\sim 50^\circ$ , before quickly diminishing for times  $t > 1/2$  s. This hotspot upper latitude spatial cutoff effect occurs whenever  $E_{th} > 0$  since the generally lower resonance energies associated with higher  $L$  shells (from (7), for a given frequency band) are thereby excluded from  $Q$ . In the present case the  $E > 100$  keV peak precipitation spot is limited to locations  $L \leq 2.6$ . Note further that the peak flux is centered generally about  $L = 2.2$ , consistent with the  $L$  shell of maximum equatorial whistler intensity (Plate 9a). In fact, preliminary review of recent multiple-path Trimp event data shows good agreement with both the  $L$ - $t$  contours of Plate 9c and the location and size of the precipitation hotspot shown in Plates 9d.1-9d.6 for lightning occurring in central Texas [Johnson *et al.*, 1999].

**4.1.3. Lightning sources at  $\lambda_s = 40^\circ$  and  $50^\circ$ , energies  $E > 100$  keV.** Plates 10 and 11 show dynamic precipitation hotspots for lightning sources at  $\lambda_s = 40^\circ$  and  $\lambda_s = 50^\circ$ , respectively, also for energies  $E > 100$  keV. For these cases the majority of the precipitated flux is deposited at higher  $L$  shells as would be expected for such higher latitude lightning. Once again, the strong whistler intensities at higher  $L$  shells combine with the generally longer interaction lengths along these field lines to markedly increase the precipitation flux intensity, spatial extent and duration as compared with the previous case. Finally, note the manner in which the shape and extent of each (red-colored) maximum flux patch in Plates 9c, 10c, and 11c selects a distinct region of the otherwise common energy flux  $L$ - $t$  signature in keeping with the common wave and particle kinematics but distinct spatial wave intensity patterns for each lightning source.

## 4.2. Precipitation Fluence

To readily compare the effect of different lightning source locations and  $E > E_{th}$  minimum energy thresholds, Plate 12 shows the fluence spatial density (time-integrated precipitation energy flux per  $\text{cm}^2$ ) arranged as three rows of three panels each, with lightning latitudes  $\lambda_s = 30^\circ$ ,  $40^\circ$ , and  $50^\circ$  increasing over the columns from left to right and minimum energy threshold values  $E_{th} = 0$ , 100 keV, and 1 MeV increasing over the rows from bottom to top, where common flux scales are used across each row. Above each plot panel is shown the total energy (in kilojoules) precipitated over the entire affected spatial region. For these equal

strength lightning discharges giving the indicated mid-band equatorial whistler intensities of  $\sim 10$  to 30 pT along the most intense ray paths (Plate 6), the total precipitated energy integrated over all particle energies ( $E > 0$ ), space and time ranges from  $E_{tot} = 1.8$  MJ for  $\lambda_s = 30^\circ$  to  $E_{tot} > 7.5$  MJ for  $\lambda_s = 50^\circ$ , per lightning discharge.

For the higher energy ranges  $E > 100$  keV and  $E > 1$  MeV, the location of the fluence peak spot tracks the lightning source in a clear monotonic fashion, increasing in latitude along with the source. Considering  $E > 100$  keV electrons specifically (center row), for the lowest latitude source ( $\lambda_s = 30^\circ$  or  $19^\circ$  geographic, center left) the separation between the lightning discharge and the precipitation fluence center is  $\sim 20^\circ$ , while for the highest latitude source ( $\lambda_s = 50^\circ$  or  $39^\circ$  geographic, center right) this separation diminishes to  $\sim 7^\circ$ , owing to the tighter field line convergence at higher  $L$  shells (cf. Plate 6, right-most column). Such convergence between lighting source and peak precipitation latitudes is in fact manifest in observations of lightning-induced electron precipitation [Lauben *et al.*, 1999].

## 4.3. Energy Flux and Electron Count Profiles

The dynamic hotspot and fluence summary plots presented in the previous sections all show a marked tendency for the precipitation energy and number fluxes to exhibit especially intense values at higher  $L$  shells and, equivalently, higher precipitation latitudes. It is of interest to summarize this poleward bias by integrating energy flux  $Q(\lambda_p, \delta, t)$  and electron number flux  $N(L, \delta, t)$  (similarly constructed from (18)) over both longitude  $\delta$  and time  $t$  to obtain profiles  $\bar{Q}(\lambda_p)$  and  $\bar{N}(L)$  over latitude  $\lambda$  and  $L$  shell, respectively, for each lightning latitude  $\lambda_s$  and energetic electron lower energy threshold  $E_{th}$ .

**4.3.1. Energy flux versus latitude.** Figure 8 gives the resulting  $\bar{Q}(\lambda)$  profiles versus latitude for lightning at  $\lambda_s = 20^\circ$ ,  $30^\circ$ ,  $40^\circ$ , and  $50^\circ$ , for  $E > 0$ ,  $E > 100$  keV, and  $E > 1$  MeV, expressed in units of Joules/degree of latitude. The curves corresponding to all energies  $E > 0$  (Figure 8a) reveal that roughly 3 orders of magnitude greater energy is delivered to  $\sim 50^\circ$  as compared with  $\sim 25^\circ$  geographic latitude (for an eastern United States mapping) nearly independent of lightning source latitude. As the minimum energy threshold  $E_{th}$  becomes nonzero, these curves flatten as shown in Figures 8a and 8b, owing to the spatial cutoff effect mentioned previously, illustrating once again how for high latitudes (Figure 8a) most of the energy delivered to the upper atmosphere is carried by large fluxes of generally lower-energy electrons, while for low latitudes the energy is carried by lesser fluxes of higher-energy electrons. Considering that the higher-energy ( $E > 100$  keV) electrons are those most likely to penetrate to the lowest altitudes to cause detectable subionospheric perturbations, experimental ob-



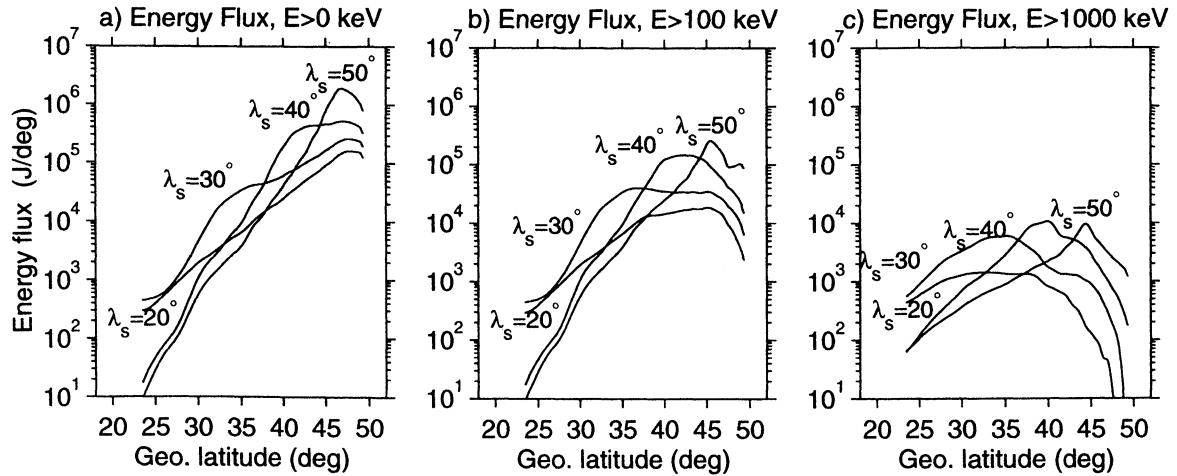


**Figure 8.** Longitude- and time-integrated precipitation energy flux profiles  $\tilde{Q}(\lambda_p)$  for energy ranges  $E > 0$ ,  $E > 100$  keV, and  $E > 1$  MeV (left to right). Each panel shows curves for each lightning source latitude  $\lambda_s = 20^\circ$ ,  $30^\circ$ ,  $40^\circ$ , and  $50^\circ$ .

servations of such LEP effects can be expected to yield profiles similar to those in Figures 8b and 8c.

**4.3.2. Electron count versus  $L$  shell.** Figure 9 gives the resulting  $\tilde{N}(L)$  distribution profiles over  $L$  shell expressed in units of  $\log e/L$  (log electron number count per incremental  $L$  shell), for the same lightning latitudes and energy ranges as the previous figure. These curves show very similar behavior to the  $\tilde{Q}$  curves; in particular, the curves for  $E > 100$  keV in Figure 9b exhibit a broad peak over  $L = 2.2 - 3.5$ , indicating that lightning-generated whistlers are most efficient at removing energetic ( $E > 100$  keV) electrons over these  $L$  shells, again nearly independent of lightning source latitude.

Figures 8 and 9 together indicate that the net effect of all the essential factors of lightning source location, latitude-dependent attenuation, resonance interaction length, energetic electron spectral hardness, etc., causes maximal precipitation regions for these  $E > 100$  keV

energies to be confined to roughly the range  $\sim 30^\circ$  to  $\sim 50^\circ$  geographic latitude (for North American longitudes), remarkably consistent with the locations of the vast abundance of Trimpi events detected over the continental United States [Inan et al., 1990], and equivalently,  $\sim 2.2 \leq L \leq 3.5$ , remarkably consistent with the location of the slot region. This result strongly motivates further in-depth study of the total impact of all global lightning activity on the trapped radiation belt populations, including contribution to the formation of the slot region.

## 5. Discussion and Conclusion

### 5.1. Related Theory and Observations

**5.1.1. Chang and Inan [1985].** Direct comparisons may be made with Chang and Inan [1985] (hereafter referred to as Chang) which presents precipitation energy flux pulses similar to those in section 3 but

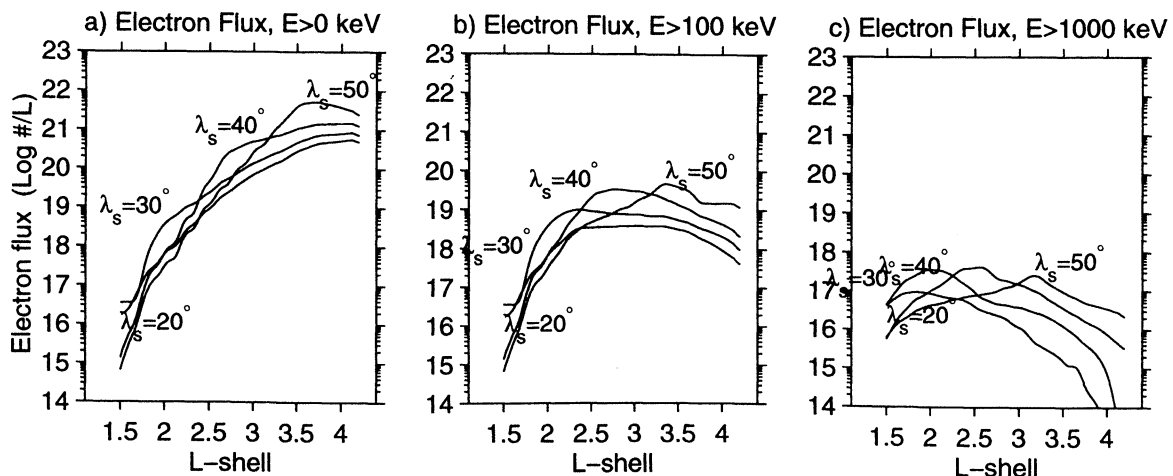


**Figure 9.** Longitude-integrated electron precipitation number flux profiles  $\tilde{N}(L)$  versus  $L$  shell. Format similar to previous figure.

for parallel-propagating (i.e., ducted, for which  $\theta_k = 0$ ) whistlers. In making these comparisons it should be kept in mind that (1) for parallel-propagating waves the resonant electron energies are somewhat lower than for oblique waves [Lauben, 1998], (2) the whistler intensities given by Chang assume a somewhat different (but roughly equivalent) input wave power spectrum, and (3) the cold plasma density model used by Chang is somewhat different, affecting the wave propagation times. Nonetheless, as a first example, at  $L = 2$  Chang's Figure 7 gives a peak flux (after scaling Chang's normalized  $\Phi_o = 1 \rightarrow \Phi_o = 1 \times 10^8$  el cm $^{-2}$  s $^{-1}$  sr $^{-1}$  keV $^{-1}$  to make comparison for identical phase-space densities  $f_v$ ) of  $\sim 0.8$  milli-erg cm $^{-2}$  s $^{-1}$  at  $t = 0.25$  s for wave intensity 2 pT at  $f = 1$  kHz (from Chang's Figure 5), while Figure 4 ( $\lambda_s = 30^\circ$ ) of the present work shows a peak flux of 1.5 milli-erg cm $^{-2}$  s $^{-1}$  at slightly earlier time  $t = 0.2$  s, which must here be adjusted downward for comparison at equal wave intensities (the present whistler model gives  $B_{y,eq}^w = 7$  pT at  $f = 1$  kHz for this case, requiring a factor of 3.5 reduction to match Chang's 2 pT), resulting in a comparative peak precipitation energy flux of 0.43 milli-erg cm $^{-2}$  s $^{-1}$ , about one-third that of the ducted case. For  $L = 3.5$ , Chang gives a peak flux (also after scaling  $\Phi_o$ ) of 9 milli-erg cm $^{-2}$  s $^{-1}$  occurring at  $t \simeq 1.2$  s for a wave magnetic field intensity of  $\sim 8$  pT at  $f = 5.1$  kHz, while from Figure 6 ( $\lambda_s = 50^\circ$ ), interpolating  $Q(t)$  profiles between  $L = 3.4$  and  $L = 3.6$  gives  $\sim 32$  milli-erg cm $^{-2}$  s $^{-1}$  at slightly earlier  $t \simeq 1$  s, which again after scaling downward (from  $B_{y,eq}^w = 30 \rightarrow 8$  pT) gives a comparative energy flux of  $\sim 8.4$  milli-erg cm $^{-2}$  s $^{-1}$ , just 7% less than that for the ducted case. Finally, at  $L = 4$ , Chang gives peak flux (after scaling  $\Phi_o$ ) just exceeding 10 milli-erg cm $^{-2}$  s $^{-1}$  at  $t \simeq 1.9$  s for wave intensity  $\sim 0.5$  pT at  $f = 1$  kHz, while the oblique whistler results (this case not shown) give 14 milli-ergs/cm $^2$ /s at  $t = 2.1$  s, which after scaling for equivalent wave intensity (from  $B_{y,eq}^w = 1.65$  pT) becomes 4.2 milli-erg cm $^{-2}$  s $^{-1}$ , just less than half that for the ducted case.

These comparisons show that in general the peak precipitation energy fluxes for oblique whistlers are within a factor of only  $\sim 2$  to 3 below those calculated by Chang for ducted whistlers having equivalent wave intensities, and in some cases are within 10% of those fluxes for ducted whistlers. This result is completely in keeping with the moderate decrease in scattering efficiency for a given wave intensity as the wave normal angle becomes nonzero [Lauben, 1998]. At the same time, given that the volume of the magnetosphere filled by any oblique whistler is vastly greater than that occupied by a ducted whistler (assumed limited to a typical duct cross-sectional size estimated to be  $\sim 0.02$  to  $0.05$   $L$ ), the total electron precipitation induced by oblique whistlers should indeed be substantial.

**5.1.2. Abel and Thorne [1998a, b].** As mentioned in the introduction, Abel and Thorne [1998a, b] have presented comprehensive diffusion rate and

equilibrium flux distribution calculations for energetic electrons in the inner magnetosphere using a classic bounce-trajectory/wave path integrated pitch angle diffusion/precipitation formulation [Kennel and Petschek, 1966; Lyons and Thorne, 1973], assuming the simultaneous presence of the three major classes of whistler-mode wave energy, namely, plasmaspheric hiss, lightning-generated oblique whistlers, and VLF transmitter signals. Although the model used to represent the oblique whistlers therein is greatly simplified by comparison (the whistlers are assigned a limited frequency range  $f = 4.5 \pm 2$  kHz, a fixed wave normal angle of  $45^\circ$  at all locations, and, to represent the total effect of all such midlatitude lightning-generated whistlers within the context of the sustained-stochastic wave field formulation, an effective occurrence rate of 3% over the particle bounce trajectories), their results indeed show that lightning whistlers significantly reduce the precipitation lifetimes for certain electron energies over certain  $L$  shell ranges.

In particular, Figure 10 of Abel and Thorne [1998a] (as well as Figure 10 of Abel and Thorne [1998b]) shows an additional order of magnitude decrease in the precipitation lifetimes of  $E = 100$  keV electrons over the range  $2.8 \leq L \leq 3.4$  (with continued effect outside this range) when lightning-generated oblique whistlers are included as a loss mechanism. This result may be related, albeit somewhat indirectly, to Figure 9b of the present work, which shows that a lightning source at similar intermediate latitude (i.e.,  $\lambda_s = 40^\circ$ ) leads to maximum  $E > 100$  keV electron flux over a similar range of  $2.5 \leq L \leq 3.3$ , while noting from Figures 5 and 6 that the rapid decrease in precipitation flux levels for energies above 100 keV evident in the  $\Phi(E, t)$  signatures indicates that the curves of Figure 9b reflect trends for energies more or less near  $E \sim 100$  keV, so that this comparison is meaningful.

**5.1.3. Voss et al. [1984, 1989].** As also mentioned previously, Voss et al. [1984] documented the first direct one-to-one association between transient energetic electron precipitation events at  $L \sim 2.2$  and individual whistlers taken to have propagated in the ducted mode. These events are also presented by Inan et al. [1989] which indicates a peak energetic electron loss cone count rate approaching  $10^4$  el s $^{-1}$ , nearly  $100\times$  the background rate of  $\sim 10^2$  el s $^{-1}$  el/s for these events, which are reported therein as being within the strongest 10% of those generally observed. By comparison, Figure 4 shows a peak count rate for  $L = 2.2$  reaching  $3 \times 10^3$  el s $^{-1}$  (for an implied idealized particle detector optimized to observe exactly the loss cone), which is thus  $30\times$  above the background flux levels observed by Voss et al. [1984]. These results suggests that oblique whistler-induced electron precipitation may well be detectable using present-day instruments, at least for strong lightning and optimum detector location with respect to the maximally affected field lines.

A comprehensive survey has been published [Voss

*et al.*, 1998] which shows that LEP pulses manifest a preferred distribution at  $2 < L < 3$  over the United States, at least for those events which can be correlated with ducted whistlers measured at ground stations. It is curious that this range in  $L$  shell shows good agreement with the broad precipitation profile peaks for  $\lambda_s = 30^\circ$  and  $\lambda_s = 40^\circ$  shown in Figure 9b. At the very least, it should be kept in mind that the emergence of a ducted whistler from the magnetosphere at some particular  $L$  shell does not preclude the concurrent propagation of an oblique-mode whistler which itself does not emerge but which nonetheless induces precipitation in accord with the present calculations. Indeed, it may be the case that the enhanced scattering efficiency associated with  $\theta_k \sim 0$  wave normals [Chang and Inan, 1985a; Lauben, 1998] maintained by the presence of an occasional duct (or inside edge of a primary or secondary plasmopause) along some particular field line simply increases the detectability for that  $L$  shell, thus leading to the high apparent correlation of strong LEP with ducted whistlers as reported by Voss *et al.* [1998]. At the same time, since as of this writing the simultaneous measurement of an LEP event along with causative whistler wave normal angle has yet to be made, it is difficult to know for certain the characteristics of those whistlers causing these observed LEP events. Indeed, recent review of existing ground-based Trimpi data [Lauben *et al.*, 1999], as well as exciting new results [Johnson *et al.*, 1999], gives indication that certain events previously attributed to ducted whistlers may have in fact been produced by oblique whistlers. These last points emphasizes the importance of further study regarding the precipitation levels and occurrence rates for LEP induced by whistlers propagating in each respective mode.

## 5.2. Conclusion

In summary, these results indicate that lightning-generated oblique whistler electron precipitation deposits appreciable energy to the upper atmosphere over widespread midlatitude geographic regions displaced universally poleward from the causative lightning source. The calculated flux levels should prove readily detectable for sufficiently strong whistler intensities and sufficient available near-loss cone energetic electron flux. Finally, these results strongly suggest that oblique whistler precipitation contributes significantly to the loss of energetic radiation belt electrons from the magnetosphere, particularly over the range  $2.2 \leq L \leq 3.5$  where the slot region forms.

## References

- Abel, B., and R.M. Thorne, Electron scattering loss in earth's inner magnetosphere, 1. Dominant physical processes, *J. Geophys. Res.*, **103**, 2385–2396, 1998a.
- Abel, B., and R.M. Thorne, Electron scattering loss in earth's inner magnetosphere, 2. Sensitivity to model parameters, *J. Geophys. Res.*, **103**, 2397–2407, 1998b.
- Angerami, J.J., and J.O. Thomas, Studies of planetary atmospheres, 1. the distribution of electrons and ions in the earth's exosphere, *J. Geophys. Res.*, **69**, 4537, 1964.
- Bell, T.F., The nonlinear gyroresonance interaction between energetic electrons and coherent vlf waves propagating at an arbitrary angle with respect to the earth's magnetic field, *J. Geophys. Res.*, **89**, 905–918, 1984.
- Bell, T.F., The wave magnetic field amplitude threshold for nonlinear trapping of energetic gyroresonant and landau resonant electrons by nonducted vlf waves in the magnetosphere, *J. Geophys. Res.*, **91**, 4365–4379, 1986.
- Brice, N., Fundamentals of vlf emission generation mechanisms, *J. Geophys. Res.*, **69**, 4515, 1964.
- Burgess, W.C., and U.S. Inan, The role of ducted whistlers in the precipitation loss and equilibrium flux of radiation belt electrons, *J. Geophys. Res.*, **98**, 15,643–15,665, 1993.
- Carpenter, D.L., and R.R. Anderson, An isee/whistler model of equatorial electron density in the magnetosphere, *J. Geophys. Res. (USA)*, *J. of Geophys. Res.*, **97**, 1097–1108, 1992.
- Carpenter, D.L., U.S. Inan, M.L. Trimpi, R.A. Helliwell, and J.P. Katsufakis, Perturbations of subionospheric lf and mf signals due to whistler-induced electron precipitation bursts, *J. Geophys. Res.*, **89**, 9857–9862, 1984.
- Carpenter, D.L., C.G. Park, J.F. Arens, and D.J. Williams, Position of the plasmopause during a stormtime increase in trapped energetic ( $E > 280$  keV) electrons, *J. Geophys. Res.*, **76**, 4669–4673, 1971.
- Chang, H.C., and U.S. Inan, Lightning-induced electron precipitation from the magnetosphere, *J. Geophys. Res.*, **90**, 1531–1541, 1985a.
- Chang, H.C., and U.S. Inan, Test particle modeling of wave-induced energetic electron precipitation, *J. Geophys. Res.*, **90**, 6409–6418, 1985b.
- Chang, H.C., U.S. Inan, and T.F. Bell, Energetic electron precipitation due to gyroresonant interactions in the magnetosphere involving coherent vlf waves with slowly varying frequency, *J. Geophys. Res.*, **88**, 7037–7050, 1983.
- Cornwall, J.M., Scattering of energetic trapped electrons by very-low-frequency waves, *J. Geophys. Res.*, **69**, 1251, 1964.
- Crary, J.H., The effect of the earth-ionosphere waveguide on whistlers, *Tech. rep.*, Stanford Univ. Radio Science Lab., Stanford, Calif., 1961.
- Cummer, S.A., and U.S. Inan, Measurement of charge transfer in sprite-producing lightning using elf radio atmospherics, *Geophys. Res. Lett.*, **24**, 1731–1734, 1997.
- Draganov, A.B., U.S. Inan, V.S. Sonwalkar, and T.F. Bell, Magnetospherically reflected whistlers as a source of plasmaspheric hiss, *Geophys. Res. Lett.*, **19**, 233–236, 1992.
- Dungey, J.W., Loss of van allen electrons due to whistlers, *Planet. Space Sci.*, **11**, 591, 1963.
- Dysthe, K.B., Some studies of triggered whistler emissions, *J. Geophys. Res.*, **76**, 6915–6931, 1971.
- Edgar, B.C., The upper- and lower-frequency cutoffs of magnetospherically reflected whistlers., *J. Geophys. Res.*, **81**, 205–211, 1976.
- Helliwell, R.A., *Whistlers and Related Ionospheric Phenomena*, Stanford University Press, Stanford, Calif., 1965.
- Imhof, W.L., J. Mobilia, H.D. Voss, H.L. Collin, M. Walt, R.R. Anderson, and J.R. Wygant, Association of waves with narrow particle dropouts in the outer radiation belt, *J. Geophys. Res.*, **102**, 11,429–11,441, 1997.
- Imhof, W.L., J.B. Reagen, H.D. Voss, E.E. Gaines, D.W. Datlowe, J. Mobilia, R.A. Helliwell, U.S. Inan, J. Katsufakis, and R.G. Joiner, The modulated precipitation of radiation belt electrons by controlled signals from vlf transmitters, *Geophys. Res. Lett. (USA)*, *Geophys. Res. Lett.*, **10**, 615–618, 1983.
- Imhof, W.L., H.D. Voss, J. Mobilia, M. Walt, U.S. Inan, and

- D.L. Carpenter, Characteristics of short-duration electron precipitation bursts and their relationship with vlf wave activity, *J. Geophys. Res.*, **94**, 10,079–10,093, 1989.
- Imhof, W.L., H.D. Voss, M. Walt, E.E. Gaines, J. Mobilia, D.W. Datlowe, and J.B. Reagan, Slot region electron precipitation by lightning, vlf chorus and plasmaspheric hiss, *J. Geophys. Res.*, **91**, 8883–8894, 1986.
- Inan, U.S., Non-linear gyroresonant interaction of energetic particles and coherent vlf waves in the magnetosphere, Ph.D. thesis, Stanford University, 1977.
- Inan, U.S., Gyroresonant pitch angle scattering by coherent and incoherent whistler mode waves in the magnetosphere, *J. Geophys. Res.*, **92**, 127–142, 1987.
- Inan, U.S., and T.F. Bell, The plasmopause as a vlf wave guide, *J. Geophys. Res.*, **82**, 2819–2827, 1977.
- Inan, U.S., T.F. Bell, and H.C. Chang, Particle precipitation induced by short-duration vlf waves in the magnetosphere, *J. Geophys. Res.*, **87**, 6243–6264, 1982.
- Inan, U.S., T.F. Bell, and R.A. Helliwell, Nonlinear pitch angle scattering of energetic electrons by coherent vlf waves in the magnetosphere, *J. Geophys. Res.*, **83**, 3235–53, 1978.
- Inan, U.S., W.C. Burgess, T.G. Wolf, D.C. Shafer, and R.E. Orville, Lightning-associated precipitation of mev electrons from the inner radiation belt, *Geophys. Res. Lett.*, **15**, 172–175, 1988.
- Inan, U.S., and D.L. Carpenter, On the correlation of whistlers and associated subionospheric vlf/lf perturbations, *J. Geophys. Res.*, **91**, 3106–3116, 1986.
- Inan, U.S., D.L. Carpenter, R.A. Helliwell, and J.P. Katsufakis, Subionosphere vlf/lf phase perturbations produced by lightning-whistler induced particle precipitation, *J. Geophys. Res.*, **90**, 7457–7469, 1985a.
- Inan, U.S., H.C. Chang, and R.A. Helliwell, Electron precipitation zones around major ground-based vlf signal sources, *J. Geophys. Res.*, **89**, 2891–2906, 1984.
- Inan, U.S., H.C. Chang, R.A. Helliwell, W.L. Imhof, J.B. Reagan, and M. Walt, Precipitation of radiation belt electrons by man-made waves: a comparison between theory and measurement, *J. Geophys. Res.*, **90**, 359–369, 1985b.
- Inan, U.S., F.A. Knifsend, and J. Oh, Subionospheric vlf 'imaging' of lightning-induced electron precipitation from the magnetosphere, *J. Geophys. Res.*, **95**, 17,217–31, 1990.
- Inan, U.S., M. Walt, H.D. Voss, and W.L. Imhof, Energy spectra and pitch angle distributions of lightning-induced electron precipitation: analysis of an event observed on the s81-1 (seep) satellite, *J. Geophys. Res.*, **94**, 1379–1401, 1989.
- Jasna, D., U.S. Inan, and T.F. Bell, Precipitation of suprathermal (100 ev) electrons by oblique whistler waves, *Geophys. Res. Lett.*, **19**, 1639–1642, 1992.
- Jasna, D., U.S. Inan, and T.F. Bell, Resonant interactions between radiation belt electrons and whistler mode waves in the magnetosphere, Ph.D. thesis, Stanford University, 1993.
- Johnson, M.P., U.S. Inan, and D.S. Lauben, Subionospheric vlf signatures of oblique (nonducted) whistler-induced precipitation, *Geophys. Res. Lett.*, **26**, 3569–3572, 1999.
- Kennel, C.F., and H.E. Petschek, Limits on stable trapped particle fluxes, *J. Geophys. Res.*, **71**, 1, 1966.
- Koons, H.C., B.C. Edgar, and A.L. Vampola, Precipitation of inner zone electrons by whistler mode waves from the vlf transmitters ums and nwc, *J. Geophys. Res.*, **86**, 640–648, 1981.
- Lauben, D.S., Precipitation of radiation belt electrons by obliquely-propagating lightning-generated whistler waves, Ph.D. thesis, Stanford University, 1998.
- Lauben, D.S., U.S. Inan, and T.F. Bell, Poleward-displaced electron precipitation from lightning-generated oblique whistlers, *Geophys. Res. Lett.*, **26**, 2633–2636, 1999.
- Lyons, L.R., and C.F. Kennel, Formation of the slot between the inner and outer electron radiation belts, *Trans. Am. Geophys. Union (USA)*, *Trans. of the American Geophys. Union*, **53**, 485, 1972.
- Lyons, L.R., and R.M. Thorne, Equilibrium structure of radiation belt electrons, *J. Geophys. Res.*, **78**, 2142–2149, 1973.
- McIlwain, C.E., Processes acting upon outer zone electrons, *Radiation Belts Models and Standards*, pp. 15–26, 1997.
- Poulsen, W.L., U.S. Inan, and T.F. Bell, A multiple-mode three-dimensional model of vlf propagation in the earth-ionosphere waveguide in the presence of localized d region disturbances, *J. Geophys. Res.*, **98**, 1705–1717, 1993.
- Rastani, K., U.S. Inan, and R.A. Helliwell, De 1 observations of siple transmitter signals and associated sidebands, *J. Geophys. Res.*, **90**, 4128–4140, 1985.
- Ristic-Djurovic, J.L., T.F. Bell, and U.S. Inan, Precipitation of radiation belt electrons by magnetospherically reflected whistlers, *J. Geophys. Res.*, **103**, 9249–9260, 1998.
- Sazhin, S.S., Landau damping of low frequency whistler-mode waves, *Annales Geophysicae. Atmospheres, Hydrospheres and Space Sciences*, **9**, 690–695, 1991.
- Schild, M.A., and L.A. Frank, Electron observations between the inner edge of the plasma sheet and the plasmasphere, *J. Geophys. Res.*, **75**, 5401–5414, 1970.
- Stix, T.H., *The Theory of Plasma Waves*, McGraw-Hill, 1962.
- Thorne, R.M., Unducted whistler evidence for a secondary peak in the electron energy spectrum near 10 kev, *J. Geophys. Res.*, **73**, 4895–4904, 1968.
- Uman, M.A., *Lightning*, Dover Publications, 1984.
- Vampola, A.L., and C.D. Adams, Electron energy deposition in the middle atmosphere, *J. Geophys. Res.*, **88**, 6267–6264, 1983.
- Vampola, A.L., and C.D. Adams, Outer zone electron precipitation, produced by a vlf transmitter, *J. Geophys. Res.*, **93**, 1849–1858, 1988.
- Van-Allen, J.A., C.E. McIlwain, and G.H. Ludwig, Radiation observations with satellite 1958e, *J. Geophys. Res.*, **64**, 271, 1959.
- Voss, H.D., W.L. Imhof, M. Walt, J. Mobilia, E.E. Gaines, J.B. Reagan, U.S. Inan, R.A. Helliwell, D.L. Carpenter, J.P. Katsufakis, and H.C. Chang, Lightning-induced electron precipitation, *Nature*, **312**, 740–742, 1984.
- Voss, H.D., M. Walt, W.L. Imhof, J. Mobilia, and U.S. Inan, Satellite observations of lightning-induced electron precipitation, *J. Geophys. Res.*, **103**, 11,725–11,744, 1998.
- Walt, M., *Introduction to geomagnetically trapped radiation*, Cambridge University Press, 1994.
- Walt, M., Source and loss processes for radiation belt particles, *Radiation Belts Models and Standards*, pp. 1–13, 1997.
- Walt, M., U.S. Inan, and H.D. Voss, Trapped electron losses by interactions with coherent vlf waves, *AIP Conf. Proc. (USA)*, *AIP Conf. Proc.*, pp. 65–70, 1996.
- Yip, W.Y., U.S. Inan, and R.E. Orville, On the spatial relationship between lightning discharges and propagation paths of perturbed subionospheric vlf/lf signals, *J. Geophys. Res.*, **96**, 249–258, 1991.

D. S. Lauben, U. S. Inan, and T. F. Bell, Starlab, Stanford University, Stanford, CA 94305-9515. (email: dsl@stanford.edu)

(Received April 30, 1999; revised December 23, 1999; accepted December 23, 1999.)